On the Formation of Gas Giant Planets Through Core Accretion

Submitted by

David A. Berardo

to

The Department of Physics
McGill University
Montreal, Quebec
May 2017

A thesis submitted to McGill University
in partial fulfillment of the requirements
of the degree of M.Sc.

Contents

Abstract

While being able to explain much of the observational data regarding giant planets, the core-accretion formation model still contains a significant amount of uncertainty regarding the initial post-formation properties of planets. The discovery of young planets implies that quantities such as the luminosity and internal structure of a newly formed gas giant must be well understood in order to properly analyse observations. In this work we attempt to quantify these properties by using the MESA stellar evolution code to calculate the formation of gas giants under a range of conditions. We study how factors such as the accretion rate and thermodynamic properties of accreted material affect the final properties of the planet.

In the past core accretion models have been subdivided into 'hot-start' and 'cold-start' models based on the luminosity of the formed planet. An implication of cold-start models is that they provide a higher estimate for a planet's mass based on its observed luminosity compared to hot-start models. We show that in all but the most extreme cases one may rule out cold-starts, finding hot-starts to be the most likely formation method. Furthermore, by applying our models to directly imaged exoplanets we find only a single peak in the posterior mass likelihood corresponding to the hot start prediction.

Abrégé

Tout en pouvant expliquer plusieurs des observations qui concernent les planètes géantes, la théorie de la formation par accrétion du noyau a encore des problèmes a expliquer les propriétés des planètes nouvellement formées. La découverte des jeunes planètes implique que des quantités telles que la luminosité et la structure interne des planètes nouvellement formées doivent être bien comprises pour pouvoir analyser correctement les observations. Dans ce travail, nous essayons de quantifier ces propriétés en utilisant le code d'évolution stellaire MESA. Nous etudions comment des facteurs tels que le taux d'accrétion et les propriétés thermodynamiques du matériel accrété affectent les propriétés finales de la planète.

Autrefois les modèles d'accrétion du noyau étaient subdivisés en des modèles de 'départs froids' et 'départs chauds' basés sur leur luminosité. En général les modèles de départs froids produisent une estimation de la masse de la planète plus haute que les modèles chauds. Nous montrons que dans tous les cas sauf les plus extrêmes les modèles chauds sont les plus probables. En plus, en appliquant nos modèles aux données des exoplanètes découvertes par imagerie directe, nous trouvons la masse la plus probable d'être celle de modèles chauds.

Acknowledgments

The work presented here has been conducted by the author as part of their Master's research, funded in part by a Fonds de recherche du Québec - Nature et technologies (FQRNT) scholarship as well as a McGill Space Institute (MSI) Trottier fellowship. This work represents original research done under the supervision of A. Cumming, part of which has been presented in the published article "Evolution of Gas Giant Entropy During Formation by Runaway Accretion" for which the author of this work was also the first author. The text in this thesis has been fully written by the author, including excerpts from the article, which benefited extensively from dicsussions with A. Cumming and G.-D. Marleau.

I would first like to thank Andrew Cumming, who has been a supportive and helpful supervisor during my MSc degree. At this early point in my graduate studies he has been invaluable in providing insight towards conducting research as well as how to succeed in an academic environment. Furthermore, thanks belong to the McGill Physics department, the MSI, and the Institute for the Research on Exoplanets (iRex) for providing an outstanding environment for conducting research as well as support and encouragement. Finally, I would like to thank my parents and the many friends and family who have been supportive of me throughout my studies and without whom I would not have made it this far.

1

Introduction

1.1 Planet Formation

Since the first confirmed detection of an extra solar planet in 1992 (Wolszczan & Frail, 1992) the field of exoplanet astronomy has progressed in leaps and bounds, with the detection now of over 3500 confirmed exoplanets [1]. With the large sample of exoplanets available to us, we can begin to tackle big picture questions such as how likely a star is to host a planet, how likely such a planet is to have earth-like orbital properties, and hopefully with the help of upcoming missions such as the James Webb Space Telescope, how likely a planet is to have favourable conditions for life.

While the search for Earth 2.0 is of great interest, it can be seen that even within our own solar system the Earth is only but a single piece of a larger ensemble. From Earth-like planets, through super-Earths (not found in our solar system), and up to ice and gas giants, the planetary zoo is populated

[1] See the online "Exoplanet Encylopedia" (Schneider et al., 2011) at http://exoplanet.eu/

with planets having masses from 0.02 $M_\oplus$(Wolszczan, 1994) to 10 M_J[2] (Marois et al., 2008), radii from 0.3 $R_\oplus$ (Barclay et al., 2013) to 2 R_J (Hartman et al., 2011), and orbital periods from ~2 hours (Bailes et al., 2011) to ~2000 yrs(Close et al., 2007) [3]. Given such a sample of specimens, one may ask how they could have formed, and more importantly how different types of planets could have co-evolved within the same planetary system. Jupiter, for example, with a mass of 318 $M_\oplus$(in units of Earth masses where 1 $M_\oplus$ = 5.98 × 10^{27}g) contains approximately 75% of the non-solar mass in our solar system and dominates its dynamics. Thus, an understanding of the formation of gas giant planets (the classification that Jupiter falls under) is critical to understanding the formation and evolution of the solar system as a whole.

There are two competing formation theories for gas giants known as "gravitational instability" and "core accretion" which consider what might happen within a protoplanetary disk composed of mm-sized dust grains. In the gravitational instability scenario, a density perturbation forms in a region of the disk. This causes the gravitational potential energy at that point to overcome the thermal energy of the particles, and the instability sets in causing the gas and dust to gravitationally collapse to form a solid and stable clump, known as a proto-planetary object (Kuiper, 1951). This is more easily done in massive disks far from the host star, where the disk is colder and rotating slower. One of the distinguishing features of this scenario is that the proto-planetary object forms on a short time-scale of 10^3 years. There a few shortcomings to this method however, such as the difficulty in forming the rocky cores of Jupiter and Saturn (Stevenson, 1982) as well as explaining the observed metallicities of these planets which are higher than solar values (Saumon et al., 1995).

Alternatively, in the core accretion scenario there is a more gradual build up of material in forming the planet (Safronov 1972; Pollack et al. 1996). Instead of a quick gravitational collapse, dust particles in the solar nebula collide and stick together to form planetesimals of typical radius ~ 0.1 km which are capable of gravitationally attracting one another (Goldreich & Ward, 1973). A core formed from planetesimals will

[2] Larger objects have been found, although it is not clear if they should be classified as planets or as brown dwarfs

[3] Throughout this work we shall use units of Earth masses ($M_\oplus$with 1 $M_\oplus$ = 5.972 × 10^{24} kg), Jupiter masses ($M_J$with 1 M_J = 1.898 × 10^{27} kg), Earth radii ($R_\oplus$ with 1 $R_\oplus$ = 6371 km) and Jupiter radii ($R_J$with 1 R_J = 6.99 × 10^4 km).

further accrete solid material at an accretion rate $\dot{M}_z$ which is initially much larger than the gas accretion rate $\dot{M}$. As the mass of the core increases so does the gas accretion rate, until a critical core mass on the order of 10 ~ 30 $M_\oplus$is reached (Mizuno, 1980), at which point runaway gas accretion occurs. Gas accretes onto the planet in free-fall, accumulating the rest of the planet's mass in the form of a gaseous envelope. Once the supply of gas has been depleted from the disk after ~ 10 Myr, accretion stops and the planet begins to cool. An important feature of this scenario is that it allows for the enriching of heavy elements through the accretion of planetesimals, which is in agreement with our solar system gas giants (Mizuno, 1980).

1.2 Post Formation Cooling of Gas Giants

Once a planet has formed, through either method, one may calculate its cooling in order to determine the luminosity of the planet at a given age (Bodenheimer & Pollack, 1986). In particular, if it is sufficiently far from its host star such that its equilibrium temperature T_{eq} given by (for a perfectly absorbing and emitting planet)

$$T_{eq} = T_\odot \left(\frac{R_\odot}{2D} \right)^{0.5} \tag{1.1}$$

is low compared to its intrinsic temperature (where $T_\odot$ and $R_\odot$ are the temperature and radius of the host star, and D is the orbital distance of the planet) then a gas giant will cool at a rate determined uniquely by its mass, composition and luminosity. This implies that a measurement of a gas giant's age and luminosity (assuming some standard composition) provides a measurement of its mass. For a planet whose luminosity is supplied by gravitational contraction, cooling takes places over the Kelvin-Helmholtz (KH) time-scale

$$t_{KH} = \frac{GM^2}{RL} \tag{1.2}$$

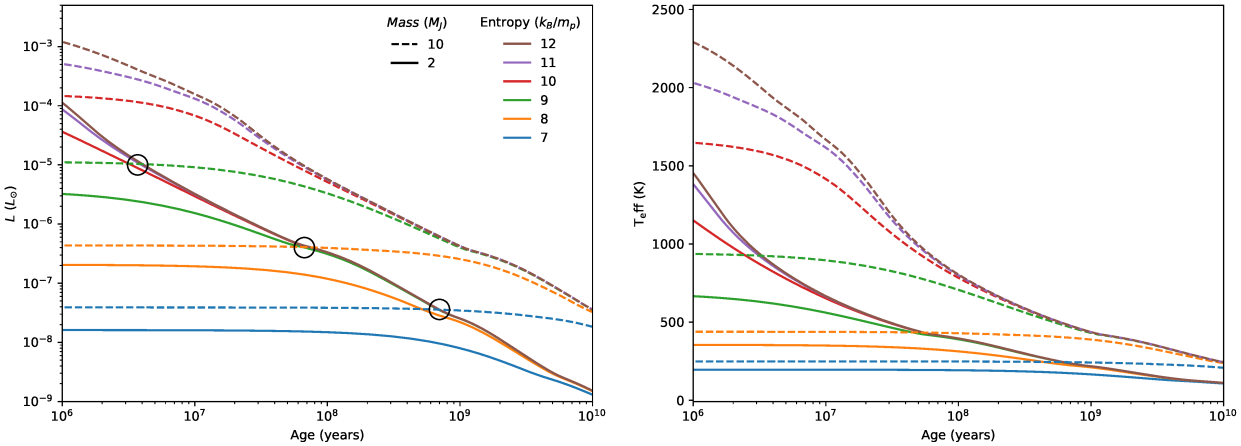

Figure 1.1: Luminosity and effective temperature for 2 M_J and 10 M_J planets as a function of time calculated using MESA (see chapter 2). The entropy value indicates the entropy of the internal adiabat at the onset of cooling. The black circles indicate where the cold starts of the 10 M_J planet intersect with the hot starts of the 2 M_J planet, showing the degeneracy of mass based on age and luminosity.

where M, R and L refer to the planet's mass, radius, and luminosity, and G is Newton's constant. While at late times a planet evolves as a thermally isolated ball of gas, at early times (relative to when accretion ended) such assumptions break down since the properties of the planet, such as its internal temperature profile or surface luminosity, may still be influenced by having been in thermodynamic contact with the proto-planetary disk. In a case where a planet forms with a large luminosity and radius, its KH time-scale is short and it quickly cools until it reaches thermodynamic equilibrium. For example, a 10 M_J object with a radius of 10 R_J and luminosity of 10^{-3} $L_\odot$ (in units of solar luminosity, where $1\,L_\odot = 3.828 \times 10^{26}\,W$) will cool over a period of $\sim 10^7$ years, after which it would be impossible to trace back its initial luminosity. These objects which quickly achieve equilibrium are referred to as 'hot starts'. In contrast, a 10 M_J object with a radius of 3 $R_J$and luminosity 10^{-5} $L_\odot$ will cool over a period of $\sim 10^9$ years. The planet takes significantly longer to 'forget' its initial conditions (i.e. its low initial luminosity), and these objects are referred to as 'cold starts'.

An example of this is shown in figure 1.1, which shows how a 10 M_J and 2 M_J planet would cool depending on their initial conditions. The cooling curves shown in this figure were created using the MESA 1-D

stellar evolution code, which is discussed in greater detail in chapter 2. The interior structure of the planet consists of an outer radiative layer and an internal adiabatic convective zone, and it is the value of the entropy of the adiabat which is used to measure how 'hot' or 'cold' the planet is (also to be discussed in chapter 2). For entropy values $\gtrsim 9\ k_B/m_p$ (in units of Boltzmanns constant per baryon mass), the curves converge to an equilibrium cooling track at ~10^8 years for the 10 M_J planet and ~10^7 years for the 2 M_J planet. For entropies below $9\ k_B/m_p$, the cooling is delayed because the KH timescale is much longer (due to the fainter luminosity of the planets).

Early formation models typically assumed a hot start so that one could ignore specific initial conditions and model the planet's cooling solely on its mass Burrows et al. (1997); Baraffe et al. (2003). This provided a direct and non-degenerate method for determining planet mass from age and luminosity. However, beginning with the detection of 2M1207b in 2004 (Chauvin et al., 2004), which has an estimated age of ~10 Myrs, we have begun to find young objects which fall into the age range where initial conditions may dominate the cooling behaviour. The implications of this are seen in figure 1.1, where black circles indicate overlap of the 10 and 2 M_J planet's cooling curves. This highlights a critical issue when attempting to derive a planet's mass from observations, since a high mass planet with a low initial luminosity is degenerate with a lower mass planet with a high initial luminosity.

1.3 Hot Start Vs Cold Start

Having stated the implications of cold and hot starts, the task at hand is now to understand the connection between the accretion process and the type of planet produced. It was first explicitly stated in Fortney et al. (2005) and Marley et al. (2007) that core accretion could lead to cold start planets. While typical hot start models produce planets with luminosities of $10^{-2} - 10^{-4}\ L_\odot$ dependent on mass, they showed that the core accretion model described in the series of papers Pollack et al. (1996), Bodenheimer et al. (2000), and Hubickyj et al. (2005) produced planets with luminosities on the order of $10^{-6}\ L_\odot$, almost completely independent of mass. One of the key ingredients in a core accretion model is the isothermal ac-

cretion shock, which occurs at the point where accreting material joins onto the planet's atmosphere (the material is initially in free-fall whereas the atmosphere is not, and so a shock will form at this boundary where properties such as density and average velocity change abruptly) (Bodenheimer et al., 2000). It is thought that the accreted material would radiate a significant amount of its kinetic energy when crossing the shock, and thus be at a lower energy when it gets incorporated into the planet resulting in the planet having a lower internal entropy. Since there is no accretion shock associated with the gravitational instability model of planet formation, this seemed to indicate a pairing of core accretion with cold starts, and gravitational instability with hot starts. This idea has a significant impact for observations to distinguish between formation scenarios, as well as providing direction for how observers should interpret the mass of such planets.

Given uncertainties in planet formation models and the potential large range in luminosity of newly formed gas giant planets, Spiegel & Burrows (2012) took the approach of treating the internal entropy of the gas giant after formation as a free parameter, producing a range of "warm starts". The predicted cooling tracks then depend on the planet mass and initial entropy. Bonnefoy et al. (2013) and Marleau & Cumming (2014) explored the joint constraint on these two parameters that can be inferred from a directly imaged planet with a known luminosity and age. For hot initial conditions, the cooling tracks depend only on the mass; cold initial conditions require a more massive planet to match the observed luminosity. Fitting hot start cooling curves therefore gives a lower limit on the planet mass. Matching the observed luminosity gives a lower limit on the initial entropy, because of the sensitive dependence of luminosity on the internal entropy (e.g. fig. 2 of Marleau & Cumming 2014). Additional information about the planet mass, such as an upper limit from dynamics, can break the degeneracy and reduce the allowed range of initial entropy.

Mordasini (2013) also identified the planetesimal surface density in the disk as a key ingredient since it sets the core mass. He simulated the growth of planets under cold- and hot-start conditions by changing the outer boundary condition for the planet during the accretion phase. In the cold case, the final entropy of the planet was found to depend sensitively on the resulting core mass through the feedback action of

the accretion shock. Most recently, Owen & Menou (2016) pointed out the potential importance of non-spherical accretion and studied the role of an accretion boundary layer in setting the thermal state of the accreted matter.

1.4 Direct Imaging of Gas Giants

As for any model, observations are required in order to confirm or deny the validity of a planet formation theory. The data we consider in this work are exoplanets discovered using the direct imaging method in which the intrinsic luminosity of a planet is directly observed as opposed to other methods which detect planets through their effects on their host star. Since a planet's luminosity is typically $10^6 - 10^{10}$ times fainter than its star, this method is biased towards finding bright planets at wide separations from their star. These conditions provide the convenience of ignoring the stellar influence on the planet's cooling. The first directly imaged planet was the previously mentioned 2M1207b found in 2004 using the Very Large Telescope (VLT). Since then, additional instruments such as the Gemini Planet Imager (GPI) have continued to provide direct imaging data of exoplanets.

The current population of directly-imaged planets shows a wide range of luminosities (e.g. Neuhäuser & Schmidt 2012; Bowler 2016), with most being too luminous to be cold starts. Examples are β Pic b with $L \approx 2 \times 10^{-4}\ L_\odot$ (Lagrange et al., 2009, 2010; Bonnefoy et al., 2013), or the HR8799 planets with $L \approx 2 \times 10^{-5}\ L_\odot$ for HR8799c, d, and e, and $8 \times 10^{-6}\ L_\odot$ for HR8799b (Marois et al., 2008, 2010). The inferred initial entropies in these cases are significantly larger than in Marley et al. (2007) (Bonnefoy et al. 2013; Bowler et al. 2013; Currie et al. 2013; Marleau & Cumming 2014). The best case for a cold start is the young giant planet 51 Eri b, which has a projected separation of 13 au from its star and $L \approx 1.4\text{–}4 \times 10^{-6}\ L_\odot$ (Macintosh et al., 2015). This luminosity is consistent with the value $\approx 2 \times 10^{-6}\ L_\odot$ predicted by (Marley et al., 2007), but it also matches a hot start for a planet mass 2–3 M_J at the stellar age $\approx 20\ Myr$. Similarly, the low effective temperature of 850 K for HD 131399Ab corresponds to a hot start mass of 4 M_J at 16 Myr (Wagner et al., 2016). Another cold object is GJ 504b, which has an effective temperature of only 510 K

(Kuzuhara et al., 2013), but indications that the star is Gyrs old imply that it may be a low-mass brown dwarf rather than a planet (Fuhrmann & Chini, 2015; D'Orazi et al., 2017).

Interesting from the point of view of testing formation models has been the discovery of protoplanets still embedded in a protoplanetary disk. For example, HD 100546 b is a directly-imaged object 50 au from its Herbig Ae/Be host with a luminosity $\sim 10^{-4}\ L_{\odot}$ (Quanz et al., 2013; Currie et al., 2014a; Quanz et al., 2015), and the star may host a second planet closer in (Currie et al., 2015; Garufi et al., 2016). Sallum et al. (2015) identified two and perhaps three accreting protoplanets in the LkCa 15 transition disk. The infrared and H α luminosities were consistent with expected accretion rates: Sallum et al. (2015) report $M\dot{M} \sim 10^{-5}\ M_J^2\ yr^{-1}$, where M and $\dot{M}$ are respectively the planetary mass and accretion rate, which agrees with typical accretion rates of $\sim 10^{-3}$–$10^{-2}\ M_{\oplus}\ yr^{-1}$ in models (e.g. Lissauer et al. 2009) for $M \sim M_J$. The young ages of these stars $\lesssim 10\ Myr$ correspond to early times when there is greater potential for distinguishing formation models (e.g. fig. 4 of Marley et al. 2007), especially since the planets could be substantially younger than the star (Fortney et al., 2005). The interpretation of the observations is complicated, however. Contributions from the environment around the protoplanet, which is likely still accreting, need to be considered, and if accretion is ongoing the accretion luminosity $L_{accr} \approx GM\dot{M}/R$, where R is the planetary radius, may dominate the internal luminosity. Nevertheless, these effects can potentially be distinguished by studying the spectral energy distribution or spatially resolving the emission. For example, observations of HD 100546 b are able to make out a point-source component (surrounded by spatially-resolved emission) with blackbody radius and luminosity consistent with those of a young gas giant (Currie et al., 2014b; Quanz et al., 2015).

In order to determine the mass of a young directly imaged planet, it must be better understood how the planet formed. While the cooling of an old ($\gtrsim 10^8$yrs) planet may be safely modelled with a hot-start (or even cold-start, since initial conditions will have been forgotten by then), for younger planets this assumption may break down if the planet was formed through a cold-start, where applying a hot-start model could incorrectly over estimate the mass by a factor of 2-5. Furthermore, planets which are observed to be still forming pose a similar and even greater challenge, rendering the traditional method

of matching a planet's age and luminosity to a hot-start cooling track useless.

1.5 A schematic for Core Accretion

We now review the progress that has been made in understanding how to model the effect of accreting material in the core accretion scenario. In figure 1.2 we show a diagram of the flow of energy and matter both within and external to the planet, described in Stahler (1988). There have been a few different approaches in the literature to modelling the unknown radiative efficiency of the accretion shock in accreting protostars and planets, which results in different assumptions about the post-shock temperature and entropy (S_0 and T_0 in Fig. 1.2).

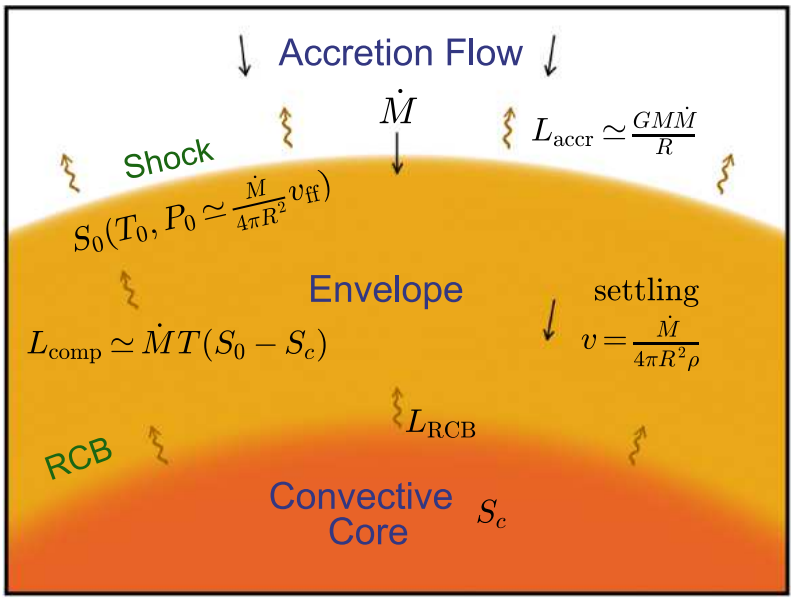

Figure 1.2: Diagram of a spherically-symmetrically accreting gas giant. Shown are the last parts of the accretion flow (*top*), the radiative envelope (*middle*), and the convective interior (*bottom*). Matter accretes onto the envelope with a rate $\dot{M}$, where it shocks and releases energy as an accretion luminosity $L_{\rm accr}$. Immediately after the shock, the matter has temperature T_0, pressure P_0 equal to the ram pressure (eq. [1.5]), and thus entropy S_0. As the material settles down through the envelope to the convective core with a velocity $v = \dot{M}/4\pi r^2 \rho$, it releases an additional luminosity $L_{\rm comp}$ from compressional heating and finally reaches the radiative-convective boundary (RCB). The convective core has entropy S_c and supplies a luminosity $L_{\rm RCB}$ to the base of the envelope.

As an outer boundary condition for the internal thermodynamic profile of the planet, we take the

temperature T_0 and pressure P_0 of the newly accreted material after it has passed through the shock. Following Bodenheimer et al. (2000), we consider an isothermal shock with density jump $\rho_2/\rho_1 = v_{ff}^2/c_s^2$, where the matter arrives at the free fall velocity

$$v_{ff} = (2GM/R)^{1/2} = 42 \text{ km s}^{-1} (M/M_J)^{1/2}(2\ R_J/R)^{1/2} \tag{1.3}$$

and c_s is the isothermal sound speed. The post-shock pressure is the ram pressure

$$P_{accr} = \rho_2 c_s^2 = \dot{M} v_{ff}/4\pi R^2 \tag{1.4}$$

or

$$P_{accr} = 3.1 \times 10^3 \text{ erg cm}^{-3} \left(\frac{\dot{M}}{10^{-2}\ M_\oplus\ yr^{-1}}\right) \left(\frac{M}{M_J}\right)^{1/2} \left(\frac{R}{2\ R_J}\right)^{-5/2} \tag{1.5}$$

where we have scaled to a typical accretion rate during the runaway accretion phase of $\dot{M} \lesssim 10^{-2}\ M_\oplus\ yr^{-1} = 1.9 \times 10^{18}\ g\ s^{-1}$ (Pollack et al., 1996; Lissauer et al., 2009).

At the low densities near the surface of the planet, the equation of state is close to an ideal gas. In appendix A we show that for a mixture of H_2 and He with helium mass fraction $Y = 0.243$ (matching the value used by Pollack et al. 1996) the entropy per baryon is

$$\frac{S}{k_B/m_p} \approx 10.8 + 3.4 \log_{10} T_3 - 1.0 \log_{10} P_4, \tag{1.6}$$

where k_B is Boltzmann's constant, m_p is the proton mass, and $T_3 \equiv T/(1000\text{ K})$, $P_4 \equiv P/(10^4 \text{ erg cm}^{-3})$. Using the ram pressure (eq. [1.5]) and assuming the gas remains molecular post-shock[4], the post-shock entropy S_0 is therefore

$$\frac{S_0}{k_B/m_p} \approx 7.4 - \log_{10}\left(\frac{\dot{M}}{10^{-2}\ M_\oplus\ yr^{-1}}\right) + 3.4 \log_{10}\left(\frac{T_0}{150\ K}\right)$$

[4] this assumption breaks down deeper in the planet, however it was found to agree in the outermost layers and so is useful in understanding the outer boundary of the entropy profile

$$-0.51\ \log_{10}\left(\frac{M}{M_J}\right) + 2.5\ \log_{10}\left(\frac{R}{2\,R_J}\right), \tag{1.7}$$

where we have scaled to the lowest possible temperature expected for T_0, the nebula temperature in Hubickyj et al. (2005). At higher temperatures, the hydrogen will be atomic post-shock, in which case the entropy is (Appendix A)

$$\frac{S}{k_B/m_p} \approx 17.2 + 4.7\log_{10} T_3 - 1.9\log_{10} P_4. \tag{1.8}$$

The maximal value of entropy we expect can be estimated by considering the temperature derived from the accretion luminosity which comes from the energy the accreted material has gained during its free fall onto the planet. If we consider the gravitational energy per mass that a parcel of accreted material carries onto the planet $\Delta E/\Delta m = GM/R$, then the rate of energy gained will be

$$L_{accr} = \frac{dE}{dt} \approx \frac{\Delta E}{\Delta m}\frac{\Delta m}{\Delta t} \approx \frac{GM\dot{M}}{R} \tag{1.9}$$

From this luminosity we can estimate a maximal temperature T_{hot} as

$$T_{hot} = \left(\frac{L_{accr}}{4\pi\sigma R^2}\right)^{1/4} \approx 3300\ K\ \left(\frac{\dot{M}}{10^{-2}\ M_\oplus\ yr^{-1}}\right)^{1/4}\left(\frac{M}{M_J}\right)^{1/4}\left(\frac{R}{2\,R_J}\right)^{-3/4} \tag{1.10}$$

which can be substituted into equation 1.8 to give a maximal entropy of

$$\begin{aligned}\frac{S_0}{k_B/m_p} \approx\ & 20.6 - 0.72\ \log_{10}\left(\frac{\dot{M}}{10^{-2}\ M_\oplus\ yr^{-1}}\right) \\ & +0.23\ \log_{10}\left(\frac{M}{M_J}\right) + 1.17\ \log_{10}\left(\frac{R}{2R_J}\right).\end{aligned} \tag{1.11}$$

We see that there is a large variation in S_0, the entropy of the material deposited at the planet surface, depending on the shock temperature. These values can be larger or smaller than the internal entropy of

the planet at the moment runaway accretion begins (which for example is $S \approx 11\ k_B/m_p$ in the simulations of Mordasini 2013). The context of these calculations are to show the range of possible outer boundary conditions that may exist during accretion, and to motivate a study of how they will ultimately dictate the properties of a fully formed planet.

1.6 Outline

The outline of the work presented in this thesis is as follows. In chapter 2, we look at how one can use MESA to model a cooling gas giant. This will involve a description of the MESA code, as well as an outline of the basic theory of stellar interiors & energy transport. In chapter 3, we extend the use of MESA to model the formation of gas giants in the core accretion scenario. The aim of this chapter will be to use a simple description of the boundary conditions during formation in order to map out the parameter space of formation conditions which lead to cold and hot starts. In particular, we try to relate the post formation internal entropy of the planet S_f (which combined with mass can provide a luminosity), to the temperature T_0 and pressure P_0 of material at the accretion shock (this work has been previously published in section 4 of Berardo et al. 2017). In chapter 4 we alter our models to use more realistic and fully time-dependant boundary conditions in order to compare our results to data of directly imaged exoplanets (this work shall be published in an upcoming paper). We attempt to place constraints on certain accretion parameters such as the accretion rate, as well as discuss the likelihood of the planets forming as either cold or hot starts. Finally in chapter 5 we conclude with a discussion of the major results that we have obtained.

2

MESA Models of Cooling Gas Giants

The goal of this chapter is to understand how the open-source 1D stellar evolution code Modules for Experiments in Stellar Astrophysics (MESA[1]) (Paxton et al., 2011, 2013, 2015) may be used to study gas giants. Before attempting to simulate the full core accretion process, we shall first describe how to make a fully formed gas giant and follow its cooling in order to demonstrate the capabilities of MESA. As well, we shall introduce certain theoretical concepts which will be useful in attempting to analyse and describe the internal structure and transfer of energy within a gas giant.

2.1 Basics of using MESA

At its core, MESA is solving the basic equations of hydrodynamics with the ability to extend to a vast range of physical effects (by incorporating different physics modules, hence its name). In practice these

[1] version 7623

equations take into account the grid structure of the model and are discretized, but written simply they are the equations of mass conservation,

$$dM_r = 4\pi\rho r^2 dr \tag{2.1}$$

where ρ and r represent density and radial distance from the center of the planet and M_r represents the total mass interior to the radius r; an equation for the conservation of momentum,

$$\frac{dP}{dM_r} = -\frac{GM_r}{4\pi r^4} - \frac{a}{4\pi r^2} \tag{2.2}$$

where P is the pressure and a is the Lagrangian acceleration. The first term on the right hand side represents hydrostatics, while the second term represents hydrodynamics (which can optionally be disabled). There is also an equation for energy conservation written as

$$\frac{dL}{dM_r} = \epsilon_{nuc} - \epsilon_{\nu,thermal} + \epsilon_{grav} \tag{2.3}$$

where L is the luminosity and ϵ_{nuc}, $\epsilon_{\nu,thermal}$, and ϵ_{grav} are the nuclear reaction energy generation rate, the specific thermal neutrino-loss rate, and the energy provided by gravitational contraction respectively.

While originally intended to study stars, it is also capable of extending down to the regime of gas giants, which behave similar in many ways to stars (minus burning hydrogen, although deuterium burning can occur for planets with masses $\gtrsim 13\ M_J$). While it is possible to include the effects of deuterium burning in MESA as an extra term in the energy equation, for simplicity we choose to study planets with a mass of at most $10\ M_J$ and so these effects are ignored.

The default installation of MESA comes with test suites containing skeleton code to study different scenarios, such as high mass planets or neutron star envelopes. For our purposes, we use the `make_planet` test suite which takes as input, among other things, an initial mass and radius. Aside from these we leave all other initial parameters at their default setting, except for irradiation which we turn off. This parame-

ter is used to simulate irradiation from a host star, however directly imaged planets are sufficiently distant ($\gtrsim$ 10 AU, see table 1 of Bowler 2016) from their host star that this can be ignored, since they would have equilibrium temperatures on the order of ~ 100-200 K, which is much lower than temperatures derived from typical internal luminosities (~ 1300 K for a 2 $R_J$planet with a luminosity of $L_{int} = 10^{-4} L_\odot$). The hydrogen and helium mass fractions are $X = 0.73$, and $Y = 0.25$ respectively, the low-temperature opacity tables are those of Freedman et al. (2008), and the equation of state is given by Saumon et al. (1995).

While MESA is capable of extending down to large gaseous planets, it still lacks the capability to model rocky objects. This limits the extent to which one can fully simulate accretion, not being able to simulate the initial phase of solid planetesimal accretion. It is however still possible to simulate a planet that includes a rocky core, which is implemented in MESA through inner boundary conditions. Using a core density and core radius specified by the user, MESA will 'cut out' the center of the model at the appropriate radius. Further details such as energy emanating from the base of the core can be specified in order to simulate, for example, energy deposition at the deep interior by accreted solid material.

2.2 Understanding MESA Output & Stellar Interiors

In order to understand how MESA may be used to model core accretion, we first look at modelling fully formed gas giants which are allowed to cool without any external influence (i.e. accretion, stellar irradiation). For the following models shown, we include a rocky core with mass and radius 10 $M_\oplus$ and 2.8 $R_\oplus$ (i.e. a mean density of 10 g cm^{-3}). We start by modelling a 1 M_J planet and in figure 2.1 visualize how its luminosity and radius evolve in time, as well as what its internal thermodynamic profile looks like.

Since this object is not generating any internal energy through nuclear burning, as expected it gets less luminous and smaller over time as it cools. We also see the internal entropy and temperature profile decrease over time. The internal entropy profile is roughly constant with depth during the planet's cooling, which is indicative of a convective interior (Hansen et al., 2012), denoted in the figure by the thicker lines. In the outermost layers of the planet there is a slight rise in entropy, indicative of a radiative zone. Since

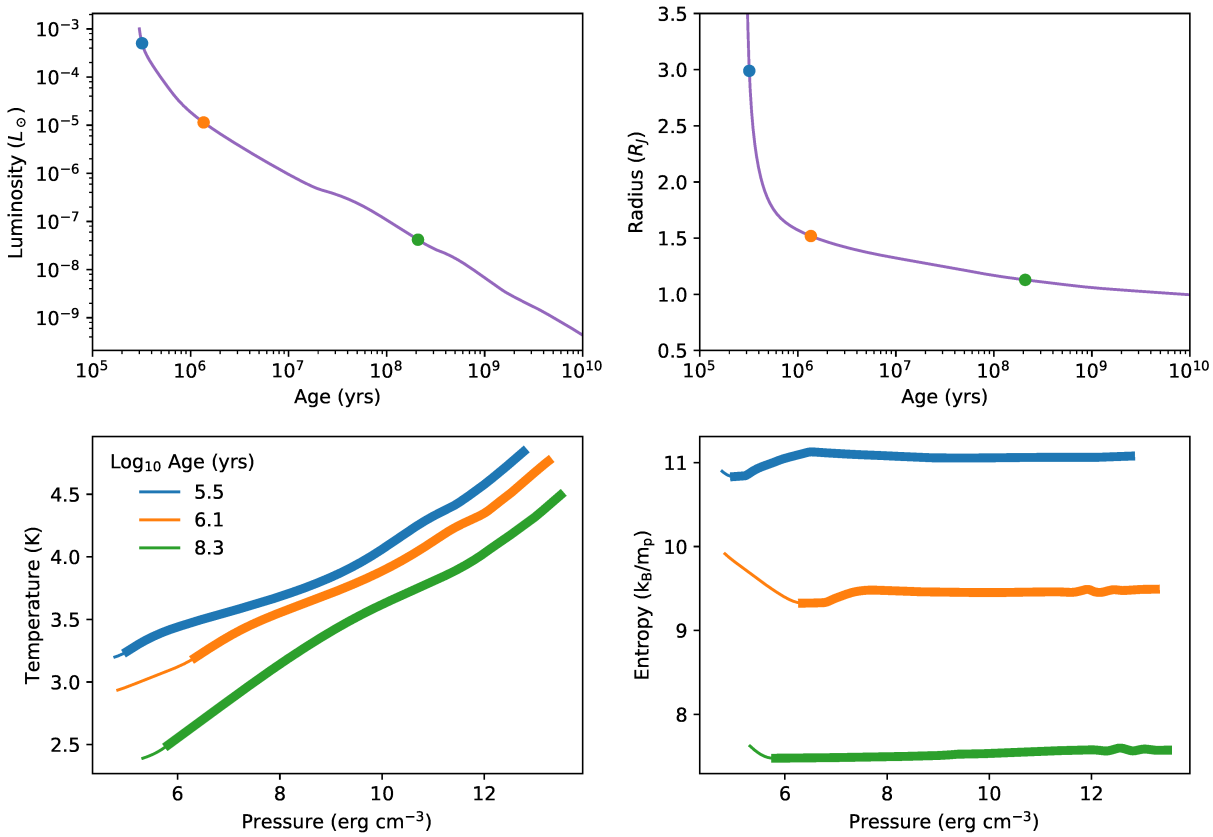

Figure 2.1: The evolution of a 1 M_J object in thermal equilibrium with its surroundings in MESA. The top left and top right panels show the evolution of the luminosity and radius of the planet over time (purple curves). The bottom left and bottom right panels show the internal temperature and entropy profiles at three different stages during the planets lifetime. The thicker section of the profiles show where convection dominates energy transport, as opposed to radiation. The points in the upper panels correspond (by color) to the times at which the profiles were taken.

the planet is at constant mass (there is no accretion or mass loss here) we see that entropy can be used to track the planets radius/temperature/luminosity (assuming a convective interior). This is important as entropy will be used a marker for hot and cold starts in the next section. It should be noted that the parameters shown in figure 2.1 are only a small subset of the parameters kept track of by MESA.

In order to better understand the evolution of such an object, it is important to understand how energy is transported within the planet which we shall do following § 4.2 of Hansen et al. (2012). First we consider

heat transport by radiation, with a luminosity at radius r within the planet given by the radiative diffusion equation:

$$L_r = \frac{-16\pi\sigma r^2 T}{3\kappa\rho}\frac{dT^3}{dr} = -\frac{64\pi\sigma r^2 T^3}{3\kappa\rho}\frac{dT}{dr} \tag{2.4}$$

where κ is the opacity, ρ is the density, σ is the Stefan-Boltzmann constant, all of which are evaluated at radius r from the center of the planet. Using the condition for hydrostatic equilibrium

$$\frac{dP}{dr} = -\frac{GM_r\rho}{r^2} \tag{2.5}$$

where M_r is the mass enclosed within radius r, We can convert the derivative to a logarithmic one by multiplying both sides by r/P to get

$$\frac{r}{P}\frac{dP}{dr} = \frac{d\ln P}{d\ln r} = -\frac{GM_r\rho}{rP} \tag{2.6}$$

and then divide both sides by the logarithmic derivative of temperature with respect to radius to get

$$\frac{d\ln P/d\ln r}{d\ln T/d\ln r} = \frac{d\ln P}{d\ln T} = -\frac{GM_r\rho}{rP}\frac{d\ln r}{d\ln T} \tag{2.7}$$

and we shall now define a quantity 'del' given by the symbol ∇ as

$$\nabla \equiv \frac{d\ln T}{d\ln P}. \tag{2.8}$$

This quantity can be combined with equations 2.4 and 2.7 to give

$$L_r = \frac{64\pi\sigma G T^4 M_r}{3P\kappa}\nabla \tag{2.9}$$

This equation is only valid in the case where radiation is the sole method of energy transportation, which in general will not be the case. The ∇ in the above equation should more properly come with a

subscript and be written as ∇_r to denote the radiative temperature gradient. Given the actual luminosity at a point within the planet, one can invert the above equation to solve for ∇_r, which is the temperature gradient that would be required for radiation to be the sole energy transport method. If the actual temperature gradient ∇ is less than ∇_r, then it can be concluded that there must some other form of energy transport present.

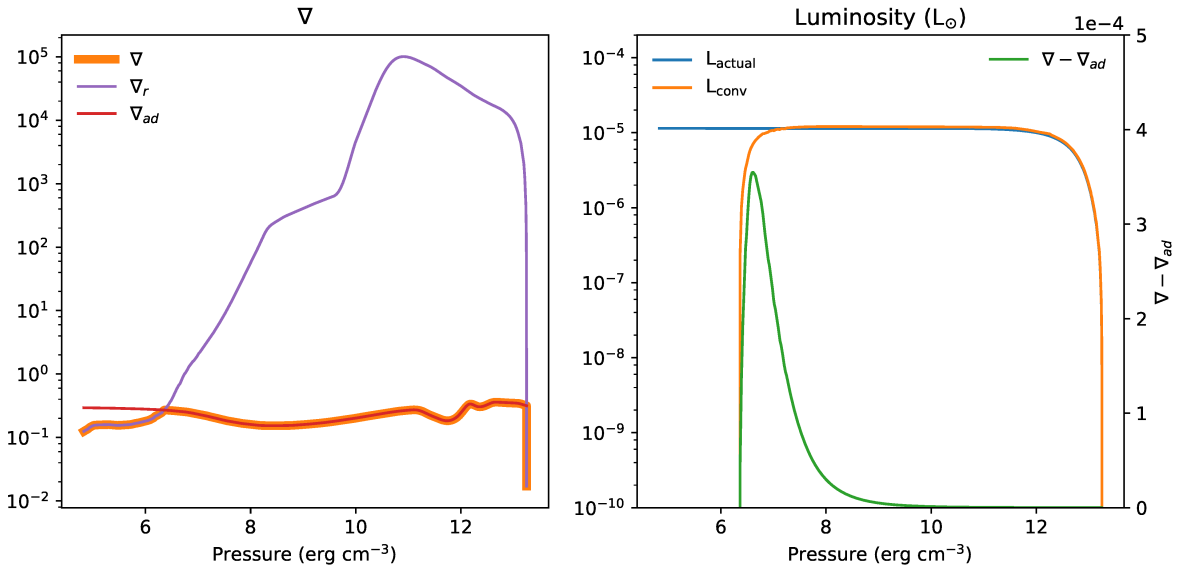

Figure 2.2: Left: A comparison of the radiative temperature gradient ∇_r to the actual temperature gradient ∇ for the same 1 M_J cooling object as was shown in figure 2.1. The profile here is when the planet was at an age of ~ 10^6 yrs, as it was for the orange profiles in the bottom two panels of that same figure. Right: The luminosity inside the planet compared to the convective luminosity as calculated by equation 2.17. Additionally, the green line shows the difference between the actual temperature gradient ∇ and the adiabatic one ∇_{ad}.

A comparison of these two gradients can be seen in figure 2.2, which is an interior snapshot of the same 1 M_J planet that was shown in figure 2.1 at an age of ~ 10^6 yrs. In the outermost portion of the planet for pressures of $P \lesssim 10^6$ erg cm^{-3}, the two values are very close and it can be concluded that in this region the planet is radiative. However the majority of the interior of the planet, which contains $\gg$99% of the mass, has $\nabla_r > \nabla$, indicating that radiation is not the source of energy transport. It can further be seen that these two regions are correlated with the internal entropy profile, seen in the bottom right panel of

figure 2.1. In the outer region where radiation dominates, there is a slight increase in entropy, but in the inner region the entropy is roughly constant.

We now introduce a third temperature gradient ∇_{ad}, describing a fluid element which is transported adiabatically (i.e. remaining in pressure equilibrium with its surroundings and having an equation of state $P \sim \rho^{\gamma}$ where γ is the adiabatic index). In appendix B we derive the criteria for a fluid to be unstable to convection

$$\nabla > \nabla_{ad} \tag{2.10}$$

which is known as the Schwarzchild criterion (Schwarzschild, 1906). If the above condition is met, then convection will be the dominant form of energy transport. It should be noted that compositional gradients within the planet will add further terms to the above inequality, resulting in the Ledoux criterion for convection (Ledoux, 1947), however we have neglected these terms by assuming a homogeneous composition. It is also shown in Appendix B that an equivalent description for a convective instability to form is

$$\frac{dS}{dr} < 0 \tag{2.11}$$

which provides a way to determine whether a region will be convective based on its entropy profile. In figure 2.1, we see that convection is indeed associated with slight negative slope in entropy, although a close examination of the entropy profile shows regions where the radial derivative of the entropy changes sign while remaining convective. This is likely due to an issue with the way that the equation of state tables are interpolated (in order to calculate entropy as a continuous function of temperature and pressure), however MESA uses equation 2.10 to determine if a region is convective. Since we see in the right hand panel of figure 2.2 that $\nabla > \nabla_{ad}$ in regions of convection, these slight deviations in entropy may be ignored.

Following the discussion in § 16.5 of Hubeny & Mihalas (2014) we are also able to calculate what the convective luminosity might be, by considering the convective flux given by

$$F_{conv} = \rho c_p \langle v \rangle \Delta T \tag{2.12}$$

where c_p is the heat capacity at constant pressure and $\langle v \rangle$ is the average convective velocity. This equation is describing the transport of energy ($c_p \Delta T$) carried by convected material ($\rho \langle v \rangle$) in the mixing length theory (MLT) prescription of convection. Since the material is transported adiabatically there is no heat loss, and so when calculating the energy transported one must take into account the difference between the temperature of the convected material relative to its surroundings, i.e.

$$\Delta T = \left[\left(-\frac{dT}{dr} \right)_{surrounding} - \left(-\frac{dT}{dr} \right)_{conv} \right] \Delta r \tag{2.13}$$

noting the extra negative signs which take into account the fact that temperature decreases outward, and so material convecting to the surface carries a positive energy flux. Considering a mixing length l we can take $\Delta r = l/2$ as an average over all fluid elements. Additionally, we consider the pressure scale height defined by

$$H_P \equiv -\frac{dr}{d \ln P} \tag{2.14}$$

and use these to rewrite the temperature difference as

$$\Delta T = \frac{T}{2} \left[\frac{1}{H_P} \left(\frac{1}{T} \frac{dT}{d \ln P} \right)_{surrounding} - \frac{1}{H_P} \left(\frac{1}{T} \frac{dT}{d \ln P} \right)_{conv} \right] l \tag{2.15}$$

$$\Delta T = \frac{1}{2} T \left(\nabla - \nabla_{ad} \right) \left(\frac{l}{H_P} \right) \tag{2.16}$$

To first order in MLT, one can take $l/H_P \sim 1$, and so the previous equation can be substituted back in equation 2.12 in to write the convective luminosity inside the planet as

$$L_{conv} = 4\pi r^2 \frac{1}{2} \rho \langle v \rangle c_P T \left(\nabla - \nabla_{ad}\right) \tag{2.17}$$

Since MESA provides all the parameters in the above equation we can calculate the convective luminosity and compare it to the actual luminosity of the planet, which is shown in the right hand panel of figure 2.2. As expected, in the regions where $\nabla > \nabla_{ad}$ there is a convective instability, and we can see that the global luminosity is equal to the convective luminosity. It should also be noted that $\nabla - \nabla_{ad} \sim 10^{-4}$ indicating only a slight departure from the background gradient is necessary for a convective instability to form. This understanding of energy transport within the planet will be critical when attempting to decipher the effects of accreting new material onto an existing planet structure.

2.3 Comparing MESA to Other Models

We now wish to generate multiple cooling models to compare them to previous results, which typically label models by their internal entropy. In MESA one cannot directly set the entropy of a planet. Instead, one must first create a planet with the desired mass and a large entropy (done by giving the planet a large initial radius). The planet is then allowed to cool until the desired internal entropy is reached[2], at which point its age is reset to the age of the planet post-accretion (say for example $\sim 10^5$ yrs for a 2 M_J planet accreting at a rate of 10^{-2} $M_\oplus$/yr. In this way we can 'artificially' construct cold and hot start planets without explicitly studying the accretion process. An illustration of this is seen in figure 1.1, where we see two planets of different masses with different initial entropies.

We now simulate cold and hot start planets with masses ranging from 1 - 10 M_J and compare the MESA models with those of Marleau & Cumming (2014). In that paper cooling curves were calculated by stepping through a pre-computed grid of planet models, parametrized by mass and entropy. Those models were in turn compared to previous results found in Spiegel & Burrows (2012) and Burrows et al. (1997). As pointed out in their work, minor constant offsets in entropy are often required in order make the mod-

[2] this is done in MESA using the `center_entropy_lower_limit` control

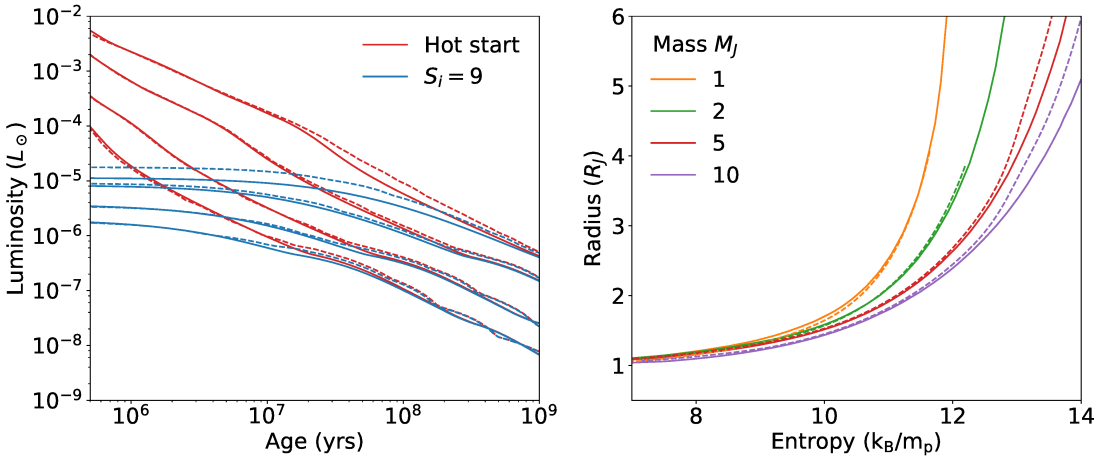

Figure 2.3: Comparison between results from MESA (solid lines) and from those of Marleau & Cumming 2014 (dashed lines). On the left is shown the cooling curves for planets with masses M = 1, 2, 5, 10 M_J increasing from bottom to top, in the case of hot start (red curves) and cold starts (blue curves). The cold start models all initially had an entropy of 9 k_B/m_p. On the right is shown the radius of the planets as a function of internal convective entropy, for different masses. For all MESA models, entropy values have been increased by a constant offset of 0.2 k_B/m_p (see text) .

els agree, and indeed here as well an offset of ~ 0.2 k_B/m_p is required for the models to agree. This offset does not represent a physical difference, since it is only differences in entropy between models which has meaning. However it can be seen in figure 2.3 that even with a constant offset there is still a difference between the different methods. In their paper they point out differences in equation of state tables as a likely cause of differences with previous work. For the cooling curves on the left plot, a constant shift in entropy would be degenerate with an offset in time, since a younger object with a lower entropy could have the same luminosity as an older object with a higher entropy. Such timing issues could arise for example from the data show in figure 2 of Marley et al. (2007) where the value of entropy is shown 1 Myr after the end of the accretion, allowing the planet a chance to cool.

Another possible explanation comes from MESA's definition of central entropy, which it takes to be the entropy value of the innermost grid point at the center of the model. Using this value to label the entire planet is only correct if the central point is at the same entropy as a large majority of the mass of the planet, which will be seen in the next section is not always the case. In place of the default central entropy

provided by MESA, we calculate the internal entropy taking a mass weighted average of the entropy of the planet (ignoring larger entropy variations at the surface which account for only a small fraction of the total mass). While it would seem in figure 2.1 that the planet is at roughly the same internal entropy, even here there can be differences of up to 0.1 by comparing the innermost entropy value to the averaged value which would already account for half of the required entropy offset. Finally, the models in Marleau & Cumming (2014) take into account deuterium burning, although since it only occurs for planets with masses $\gtrsim 13\ M_J$this could not be the case for the offset with our models.

3

Simulating Core accretion in MESA

The work presented in this chapter has been previously published in the Astrophysical Journal, in section 4 of Berardo et al. (2017) which was written by the author of this thesis. It has been reproduced here with the permission of both co-authors A. Cumming and G.-D. Marleau.

Having described the functionality of MESA as well as energy transport within a planet/star, we now attempt to tackle the problem of simulating core accretion in MESA. As previously mentioned, the core accretion scenario consists of several distinct steps. The first of these, in which solid planetesimals accrete to form the rocky core, is beyond the reach of MESA's capabilities and so this means that we can only begin at the point when runaway gas accretion occurs, roughly when the envelope mass is equal to the core mass (Mizuno, 1980). With this limitation in mind, we are able to define the specific questions which we are capable of answering, which are as follows. As the planet accumulates new matter, how does its internal profile change over time, and more importantly what does it like at the end of accretion as it

begins to cool? During runaway gas accretion material approaches the planet in free fall, passing through an accretion shock before joining onto the planet's atmosphere where it will have new thermodynamic properties due to energy loss when crossing the shock. It is the properties of the gas post-shock which are relevant for understanding how the interior of the planet will evolve. We describe the post-shock gas as having a temperature T_0 and a pressure P_0, which shall be used as outer boundary conditions when solving the fluid equations in order to determine the internal structure of the planet. The scenario described here is appropriate for a 1-D model of accretion, however the geometry of disk fed-accretion may be such that the accretion does not proceed in the same way over the entire planet. Studies such as Owen & Menou (2016) indicate additional effects such as in increase of the planet's radius due to accretion which we do not include here.

While previous work has generally chosen some prescription for the outer boundary conditions (such as choosing the temperature of the gas to be proportional to the accretion luminosity), we will instead leave both T_0 and P_0 as parameters which shall be used to map the the parameter space of possible accretion scenarios onto the parameter space of formed planets (i.e. the spectrum of cold to hot starts). Since it is impossible to model solid accretion in our framework, we instead begin our models at a point just past the end of that phase which means that certain assumptions must be made regarding what the planet might look like at this point. In the core accretion models of Mordasini (2013), the entropy of the planet at the onset of runaway accretion is $\approx 11\ k_B/m_p$. To explore the sensitivity to the initial entropy S_i, we consider values of $S_i = 9.5$, 10.45 and 11.6 k_B/m_p (recall that entropy cannot be directly set, only the initial radius, hence the non uniform values of entropy). At these values of entropy, the `make_planet` module has difficulty converging for masses as low as the crossover mass $\lesssim 0.1\ M_J$ because the planet is greatly inflated. To alleviate this problem, we instead start with larger masses of 0.2, 0.5, and 1 M_J for $S_i = 9.5$, 10.45 and 11.6 k_B/m_p, respectively. For these three choices of initial mass, we set the radius in `make_planet` to $R = 2$, 5, and 10 R_J, which leads to the desired entropy at the onset of accretion.

3.1 Accretion and the Outer Boundary Conditions

We now turn on accretion using the `mass_change` control to specify an accretion rate. By default, MESA accretes material with the same thermodynamic properties (i.e. temperature, density and thus entropy) as the outer layers of the model. This is a useful comparison case which we will refer to as 'thermalized accretion'. To model a more general case of runaway gas accretion, we use the `other_atm` module of the `run_star_extras` file in MESA in order to specify T_0 and P_0 (see Appendix C). They can be set for example to constant values for the entire evolution, or adjusted depending on the state of the planet at any given time (e.g. the mass- and radius-dependent ram pressure given by eq. [1.5]).

If the deviation from thermalized accretion is too large, MESA may fail to converge and not produce a model. The reason for this is that MESA will first create the planet with the correct mass and radius, which will be by set the outer boundary to some appropriate temperature and pressure by solving the hydrostatic fluid equations. Once this is done, then MESA will take into account the new boundary conditions, and so if the jump in say temperature is too large MESA will fail. To alleviate this, in the scenario where the imposed surface temperature is too high, we slowly increase the temperature from a lower value that does converge to the desired temperature over a timescale on the order of ~ 1% of the total accretion time to ensure that the final results are not significantly affected. For example, a model accreting at a rate of $10^{-2}\ M_\oplus\ yr^{-1}$ with a desired surface temperature of 2500 K will instead begin with 1500 K and linearly increase the temperature up to 2500 K over the course of 5000 yr.

We do not include any internal heating from planetesimal accretion. Planetesimals can deposit energy deep inside the planet, with maximal luminosity when they penetrate to the rocky core (e.g. see discussion in § 5.7 of Mordasini et al. 2015). The luminosity is $L_Z = (GM_c/R_c)\dot{M}_Z \approx 10^{-6}\ L_\odot\ (\dot{M}_Z/10^{-5}\ M_\oplus\ yr^{-1})$, where $\dot{M}_Z$ is the accretion rate of planetesimals and we take a core mass $M_c = 10\,\mathrm{M}_\oplus$ and mean core density $\bar{\rho}_c = 5\ \mathrm{g\ cm^{-3}}$. Because it is deposited potentially deep inside the convection zone, this luminosity can heat the convection zone from below and cause its entropy to increase. However, the internal luminosities we find are all much greater than L_Z, except for the coldest cases, and so we neglect this heat source.

As a check that the MESA calculations are converging to a physical model, we increased and decreased by a factor of two the `mesh_delta_coeff` parameter, which controls the length of the grid cells, and find no discernible difference in the results. Similarly, we lowered by an order of magnitude the `varcontrol_target` parameter, which controls the size of the time step, and again found no difference.

3.2 Identification of accretion regimes

We first survey the final entropies and luminosities obtained by holding T_0 and P_0 fixed during accretion. We construct a grid of models with T_0 and P_0 ranging from 100 to 2700 K (roughly spanning from typical nebula temperatures up to a planet heated by accretion luminosity) and $10^{2.3}$ to $10^{5.5}$ erg cm^{-3} (centered around the ram pressure eq. [1.5]) respectively. For these values the surface entropy S_0 ranges from $\approx$ 6 to 20 k_B/m_p (see Appendix A). In this section, we use an accretion rate of 10^{-2} $M_\oplus$ yr^{-1}, an initial mass of 0.5 M_J, and an initial entropy of 10.45 k_B/m_p.

The results of this survey are shown in Figure 3.1. We find that the final entropies can be separated into three different regimes. The black line on the right shows where the final entropy of the planet at the end of accretion is equal to the initial entropy. In the region to the right of this line the final entropy is greater than the initial entropy, hence the 'heating' regime. In the region to the left of this line, the final entropy is lower than the initial entropy, and this can be further subdivided into two more regions.

The black line in the left of Figure 3.1 shows where the final entropy of the planet is equal to the value it would reach under thermalized accretion, in which the accreted material has the same thermodynamic properties as the planet. In a sense, this scenario allows the planet to cool while increasing its mass. The final entropy reached under this conditions is referred to as $S_{\rm therm}$. It can be seen that in most cases, if $S_0 > S_{\rm therm}$ then the final entropy of the planet will be between S_i and $S_{\rm therm}$, in the 'stalling' regime, since the planet has not cooled as much as it could have. To the left of the leftmost black line, we have the region where $S_f < S_{\rm therm}$, which is again characterized by having $S_i < S_{\rm therm}$. In this 'cooling' regime, the planet cools by a greater amount than it would have and thus ends up at a lower final entropy.

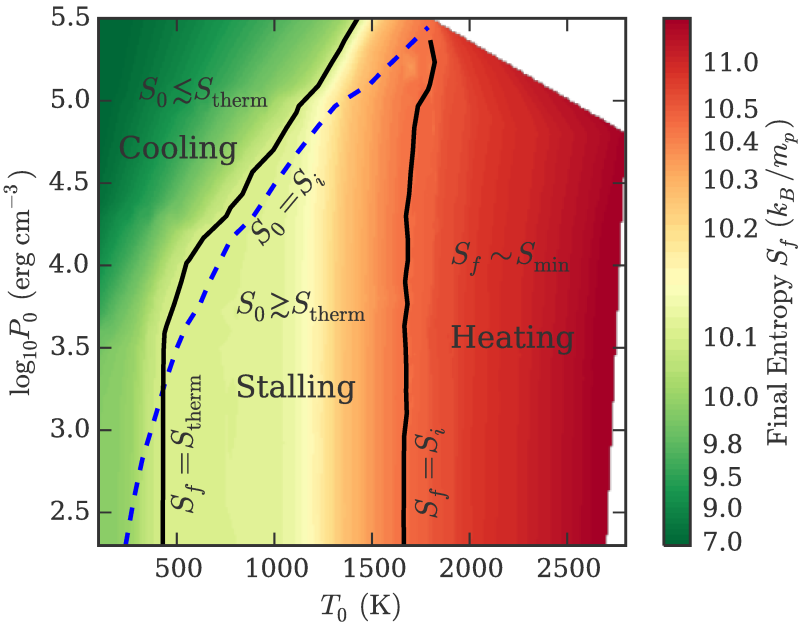

Figure 3.1: Final entropy (*colorscale*) of a 10 M_J planet accreting at 10^{-2} $M_\oplus$ yr^{-1} as a function of surface temperature T_0 and pressure P_0, held constant. Every model begins with a mass of 0.5 M_J and an initial entropy of $S_i = 10.4\ k_B/m_p$. The black line on the right indicates where the final entropy S_f is equal to S_i. The black line on the left indicates where the final entropy is equal to the entropy reached by thermalized accretion $S_{\rm therm} = 10.1\ k_B/m_p$. The blue dashed line indicates where the surface entropy S_0 is equal to the initial entropy. The three accretion regimes ("cooling", "stalling", and "heating") are discussed in the text. The colors and contours were obtained by smoothing an appropriately-distributed set of 989 independent models.

In Figure 3.2, we look at the internal profiles for planets accreting in each regime at different points throughout their accretion, in order to understand what drives their evolution. The top left panel shows the evolution under 'cooling' accretion conditions, where the surface entropy is at a value of $S_0 \approx 8.7\ k_B/m_p$, which is below $S_{\rm therm} = 10.1\ k_B/m_p$. We see the internal entropy decreases rapidly, approaching the surface entropy S_0 after accretion of about one Jupiter mass or about 30,000 years.

The bottom left panel of Figure 3.2 shows the *stalling* regime, in which the surface entropy is higher than $S_{\rm therm}$, but still low enough to smoothly attach to the interior of the model. A radiative region forms in the outer layers, which pushes the radiative convective boundary (RCB) to higher pressures, reducing the luminosity from the convective core. The internal entropy still decreases, but at a slower rate than in the cooling scenario or thermalized accretion (a similar effect as the irradiation of hot jupiters by their

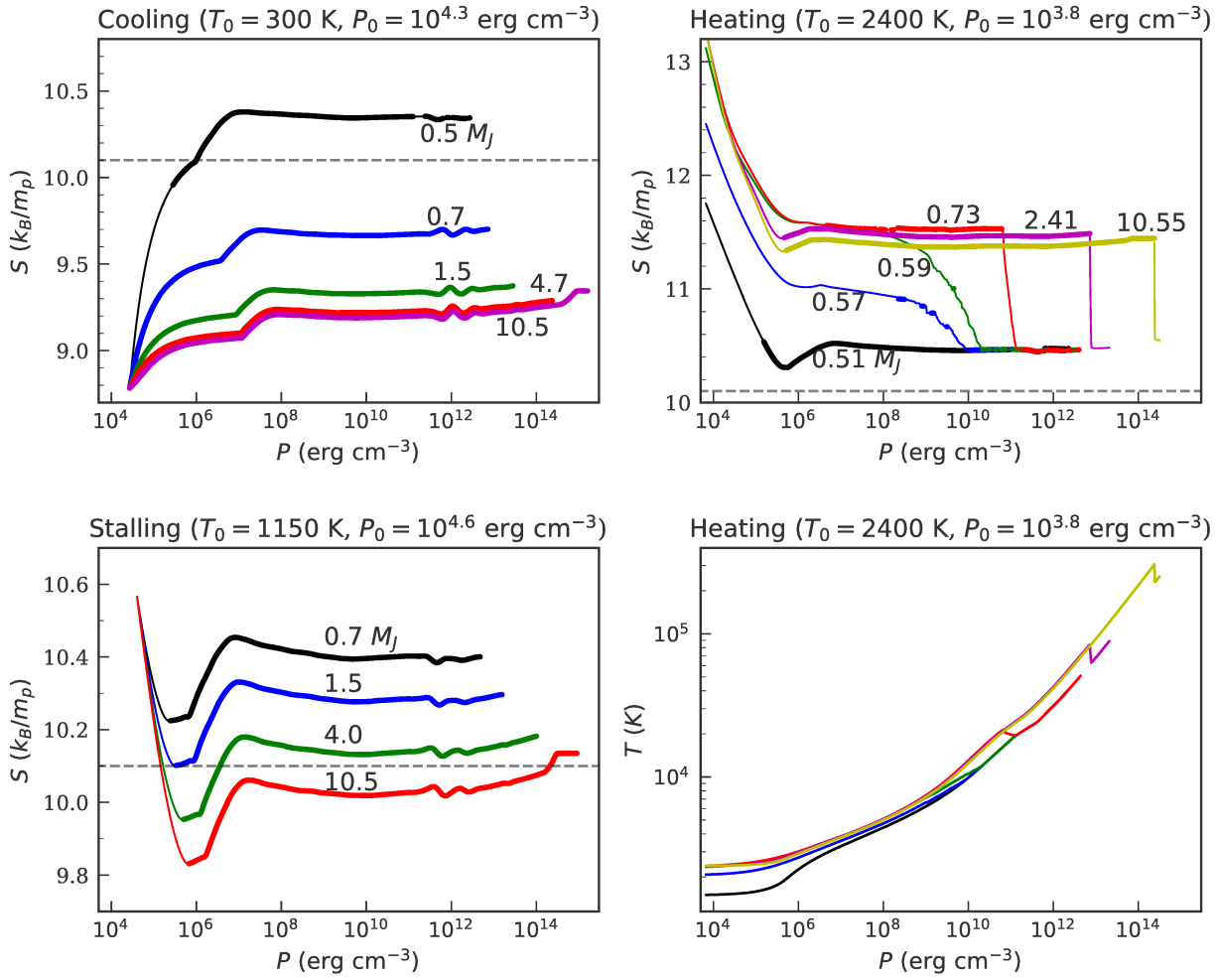

Figure 3.2: Internal entropy profiles for a planet with initial entropy $S_i = 10.45\ k_B/m_p$ undergoing accretion with boundary conditions (T_0 and P_0). They are chosen to correspond to the three accretion regimes identified in Figure 3.1 (*see panel titles*), with entropies for the accreted material of respectively $S_0 = 8.7$, 10.6, and 13 k_B/m_p for the cooling, stalling, and heating regimes. The dashed black line indicates $S_{therm} = 10.1\ k_B/m_p$. The total mass (*labels next to curves*) is used to track the time evolution of the models from 0.5 to 10.5 M_J. Convective regions in the profiles, according to the Schwarzschild criterion, are shown by thick lines. Note that each panel uses a different scale on the vertical axis. For the heating regime, in the bottom right panel the internal temperature profile is shown in addition to the entropy profile in the top right.

host star).

The top right panel of Figure 3.2 shows the *heating regime*, in which the difference in entropy between the surface and interior is too large for the envelope to accommodate. For these models, there appears to be

a minimum surface entropy S_{min} above which the planet accretes in the heating regime (see § 3.3 in Berardo et al. 2017[I]). In such a case, the accreted material accumulates to form a second convection zone above the original convective core, at the higher entropy of the accreted material. Note that there is a temperature inversion, shown in the bottom right panel, associated with the jump between the original low convective entropy zone and the new, higher-entropy convection zone; a similar temperature inversion was seen for strongly-irradiated hot jupiters by Wu & Lithwick (2013). The conduction timescale in the planet interior is very long, so that the temperature inversion remains at the same mass coordinate as accretion proceeds. As previously mentioned, the surface temperature is increased linearly from 1500 K to 2400 K over the course of 5000 years to help convergence. This gives the initial rise of the surface entropy for $M \lesssim 0.7\ M_J$.

To see how the boundary conditions determine the post-accretion planet properties, Figure 3.3 shows the final interior entropy S_f as a function of the surface entropy S_0 for a final planet mass of 10 M_J. In the hot models that develop two internal convection zones, we choose the higher internal entropy value since most of the mass of the planet is at this higher entropy value. This in turn is due to the upper zone appearing sufficiently early in the accretion history; for instance, in Fig. 3.2, only the inner $\approx 0.5\ M_J$ are frozen in at $S \approx S_i = 10.45\ k_B/m_p$.

Models with $S_0 < S_{\rm therm}$ (to the left of the dashed vertical line in Figure 3.3) are in the cooling regime. They show that the amount of cooling at a given value of surface entropy S_0 depends on the explicit choice of P_0 and T_0. Also, in this regime there is a stronger dependence on pressure than on temperature. For a fixed surface entropy, moving the surface to higher pressure means that the entropy must increase at a faster rate to match onto the internal value, implying a larger value of $\nabla - \nabla_{ad} \propto dS/dP$ and therefore a larger convective luminosity (eq. [2.17]). A higher surface pressure therefore gives more rapid cooling, resulting in a lower value of S_f at the end of accretion. It should be noted that cooling below 9 k_B/m_p requires high pressures ($P_0 > 10^{4.2}$ erg cm^{-3}) and low temperatures ($T_0 < 450$ K).

For $S_0 > S_{\rm therm}$, we see the stalling and heating regimes. In the heating regime, the final entropy

[I] This was omitted from this thesis since it involved a significant amount of work done by the co-author of Berardo et al. 2017.

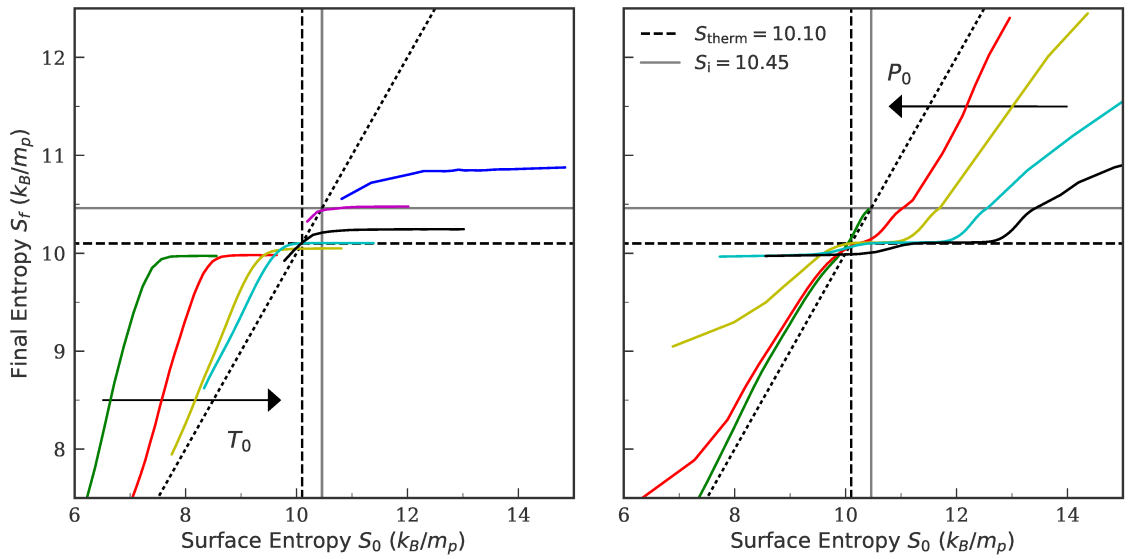

Figure 3.3: *Top panel:* Final internal entropy of the planet as a function of the entropy of the accreted surface material. The models are as in Figures 3.1 and 3.2. For structures with two convective zones, the entropy of the upper zone is used, as discussed in the text. The colored lines correspond to constant values of the shock temperature T_0 = 100, 150, 300, 450, 1350, 1750, 2100 K (*bottom left to top right*). Along each constant-T_0 curve, the surface pressure P_0 decreases from left to right. Displayed are also the value of the initial entropy of the model (S_i = 10.46 k_B/m_p; *solid gray line*) and the final entropy reached with thermalized accretion (S_{therm} = 10.10 k_B/m_p; *dashed black line*). The diagonal dotted line shows where the final and surface entropy are equal. *Bottom panel:* Same results as in the top panel but plotted as curves of constant shock pressure P_0 for $\log_{10}(P_0/\mathrm{erg\,cm^{-3}})$ = 2.3, 3.2, 4.1, 4.8, 5.5 (*top right to bottom left*); along each curve, the shock temperature T_0 increases from left to right.

lies above the initial entropy, and increases with T_0, having almost no dependence on P_0. In the stalling regime, the final entropy lies between the initial value S_i and $S_{\rm therm}$. As T_0 increases in the stalling regime, the RCB is pushed to higher pressure, reducing the luminosity at the RCB and delaying the cooling further so that the final entropy of the planet is approximately equal to the initial entropy S_i. This is a similar effect to the delayed cooling of irradiated or Ohmically-heated hot jupiters (e.g. Arras & Bildsten 2006; Huang & Cumming 2012; Wu & Lithwick 2013). In this regime, the degree of cooling is insensitive to P_0 because the envelope is close to isothermal (e.g. see Fig. 3.2), so that it is the temperature of the envelope set by T_0 that determines the RCB location. Another way to understand this is that if the outer radiative envelope were to be truncated at some pressure point, the RCB would still be in the same location and the cooling would be unaffected, whereas changing the temperature has the more drastic effect of changing

the temperature profile.

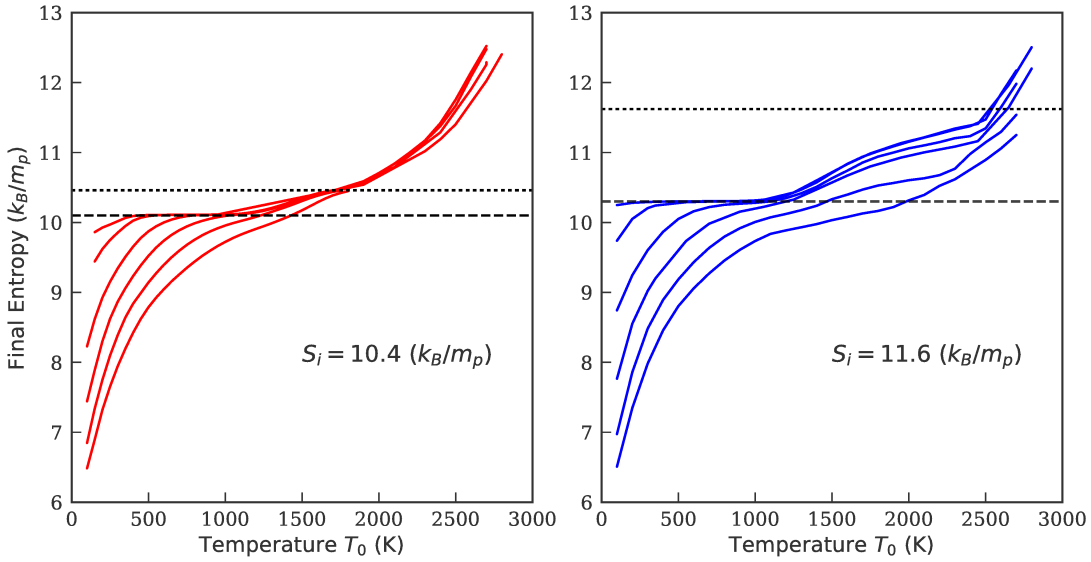

Figure 3.4: The final internal entropy two planets accreted up to a mass of 10 M_J as a function of surface temperature during accretion T_0. The left and right panels indicate planets which had an initial internal entropy of S_i = 10.4 k_B/m_p and 11.6 k_B/m_p respectively. For both cases, the solid lines represent values of constant surface pressure P_0 for $\log_{10}(P_0/\mathrm{erg\ cm^{-3}})$ = 3.7, 4.0, 4.4, 4.8, 5.1, 5.5 decreasing from the bottom most curve upward. The lower dashed lines in both panels show the value of S_{therm}, while the upper dashed lines represent the initial entropies S_i.

Additionally, the same grid of T_0 and P_0 was run for an initial entropy $S_i = 11.5\ k_B/m_p$. The difference in outcomes between the two values of initial entropy are shown in figure 3.4. The final entropy reached under thermalized accretion was similar in both cases, since for high initial entropies this value will be set by the amount of time available to cool (which also explains why for the higher value of initial entropy S_{therm} is slightly higher). Since the heating/stalling boundary is located at the initial entropy, this only increased the 'height' of the stalling regime, i.e. the distance between the horizontal lines in Figure 3.3. An important effect of this, however, is that the stalling regime occurs for a larger temperature range for the planet with a higher initial entropy. In both cases, once they have entered the heating regime the loss of dependence on pressure can be seen by the lines of constant pressure collapsing onto a single track.

In order to model runaway accretion, we now use the ram pressure P_{accr}, given by equation (1.5), as the outer boundary pressure P_0. The ram pressure evolves with time as the mass and radius of the planet change. We hold the outer temperature T_0 constant. In reality the shock temperature will also depend on mass and radius and change with time, but without a specific model for now we leave it as a constant parameter describing the post-shock conditions (a time dependent boundary temperature shall be considered in the following chapter).

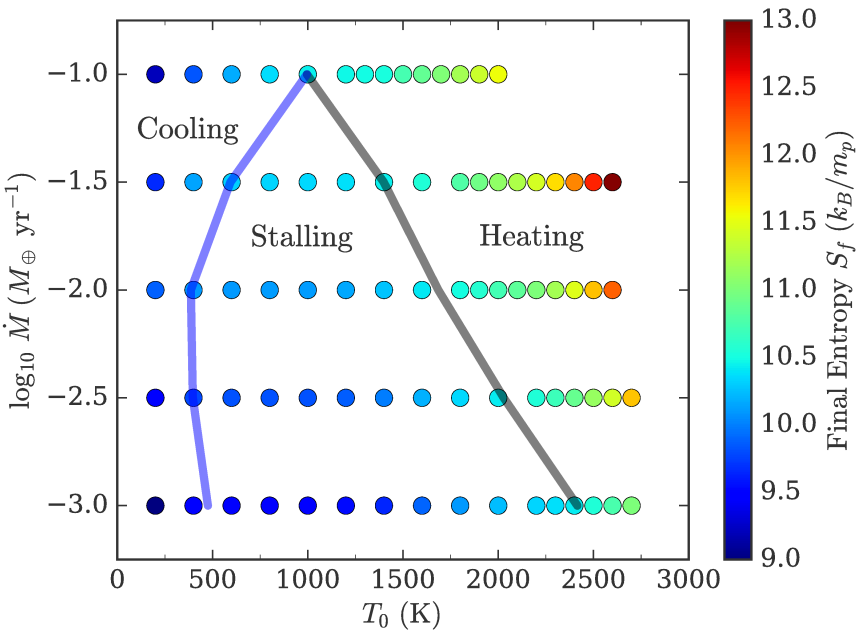

Figure 3.5: Final internal entropy (*colorscale*) of the planet as a function of shock temperature T_0 and accretion rate $\dot{M}$. The solid black line indicates the initial entropy of the models (here $S_i = 10.45\ k_B/m_p$), thus delineating the stalling and heating regimes. The solid blue line indicates the final internal entropy reached under thermalized accretion, separating the cooling and stalling regimes. This value depends on the accretion rate, so that along the blue line the entropy value changes.

Figure 3.5 shows the final internal entropy of the planet as a function of T_0 and $\dot{M}$, having started with entropy $S_i = 10.45\ k_B/m_p$. Due to the ram pressure being dependent on the accretion rate $\dot{M}$, we now switch to $\dot{M}$ and T_0 as the free parameters which we use to label different accretion scenarios. Regarding

this change, this figure is conceptually identical to figure 3.1, and we again see the separation into three accretion regimes. The blue line is drawn such that the entropy along it is at the value that would be reached by thermalized accretion at each accretion rate. The entropies to the left of the blue line are smaller, indicating the cooling regime. The black line is drawn such that the entropy along it is equal to the initial entropy. The entropy to the right of the black line are greater, indicating the heating regime. Between the blue and black lines, where the entropy lies between the initial value and the value reached by thermalized accretion, is the stalling regime. It is interesting to note that in this case, for large enough accretion rates the boundaries for the cooling and heating regimes converging, implying the loss of the stalling regime.

In the cooling regime, the entropy reaches a minimum of ~ 9 k_B/m_p, whereas we found much lower values in § 3.2. The difference is due to the fact that the ram pressure never gets high enough to decrease the surface entropy significantly. For example with $\dot{M} = 10^{-2}\ M_\oplus\ yr^{-1}$ and a final radius $R \approx 1\ R_J$ and mass $M = 10\ M_J$, the ram pressure is always $P_{\rm accr} \lesssim 10^4\ {\rm erg\ cm^{-3}}$ since $P_{\rm accr} \propto M^{1/2}R^{-5/2}$ (eq. [1.5]); comparing to Figure 3.3, this does not lead to significant cooling.

The internal entropy in the cooling regime depends in a non-monotonic way on the accretion rate. Increasing the accretion rate from 10^{-2} to $10^{-1}\ M_\oplus\ {\rm yr^{-1}}$ yields a lower entropy because the ram pressure is higher for a higher accretion rate, leading to a larger luminosity (Fig. 3.3). At lower accretion rates $\dot{M} \gtrsim 10^{-3}\ M_\oplus\ {\rm yr^{-1}}$, the luminosity is smaller than at $\dot{M} \gtrsim 10^{-2}\ M_\oplus\ {\rm yr^{-1}}$, but the accretion timescale is much longer so that more cooling can occur and the final entropy decreases with decreasing $\dot{M}$. For $\dot{M} \gtrsim 10^{-2}\ M_\oplus\ {\rm yr^{-1}}$, the boundary between the cooling and stalling regimes is at larger temperature for larger accretion rate. This is because the ram pressure is larger, and a higher temperature is needed to have a large enough entropy to be in the stalling regime. For $\dot{M} \lesssim 10^{-2}\ M_\oplus\ {\rm yr^{-1}}$, the boundary temperature is almost independent of accretion rate, because the boundary moves to low pressure (horizontal parts of the curves in the top panel of Fig. 3.3).

In the stalling regime, the final entropy increases with accretion rate because there is less time available to cool, and increases with temperature because a hotter envelope reduces the cooling luminosity. In the

heating regime, the final entropy is set by S_{min}, which increases with temperature and accretion rate. The boundary between the stalling and heating regimes can be understood by finding the temperature for which $S_{min} \approx S_i$ at each $\dot{M}$.

Figure 3.6 shows, for different values of S_i, $\dot{M}$, and T_0, the dependence of the internal entropy on planet mass, i.e. the post-formation, initial entropy ('initial' in terms of the pure cooling phase; e.g. Marley et al., 2007). In each panel, the blue dot shows the initial mass and entropy. For the cooling cases, the curves drop rapidly with increasing mass at first but then flatten at larger masses. Most of the cooling happens by the time that they have reached $\approx 4\ M_J$ (as can also be seen in the entropy profiles in Fig. 3.2). The models in the heating regime show a final entropy that depends only slightly on total mass ($\Delta S \approx 0.2\ k_B/m_p$ from 1 to 10 M_J at a given T_0). In these cases, immediately after accretion starts the hot envelope deposits matter with entropy S_{min} in a second convection zone as described in the § 3.2. In § 3 of Berardo et al. (2017), it is shown that S_{min} decreases with planet mass, so that very quickly the planet enters the stalling regime where the accreting envelope joins smoothly onto the high-entropy outer convection zone. This lets internal entropy decrease slightly with planet mass after the initial rise. This result differs from the hot-start accretion models of Mordasini (2013), which show an increasing entropy with mass and thus yield with the cold starts a tuning-fork shape.

A larger initial entropy acts to shift the final entropy upwards. If the shift is large enough it can push a model that was once in the stalling regime into the cooling regime. An example of this is the case of $\dot{M} = 10^{-3}\ M_\oplus\ yr^{-1}$ and $T_0 = 2000$ K, which is in the stalling regime for $S_i = 9.5\ k_B/m_p$ and in the cooling regime for $S_i = 11.5\ k_B/m_p$.

3.4 Cold or Hot Starts?

The luminosity of the planet after formation L_p is shown in Figure 3.7. We calculate this luminosity by taking the internal entropy at the end of accretion (for the hot cases, this is the entropy in the hotter, outer convection zone) and constructing a new planet with the same mass and internal entropy in MESA. This

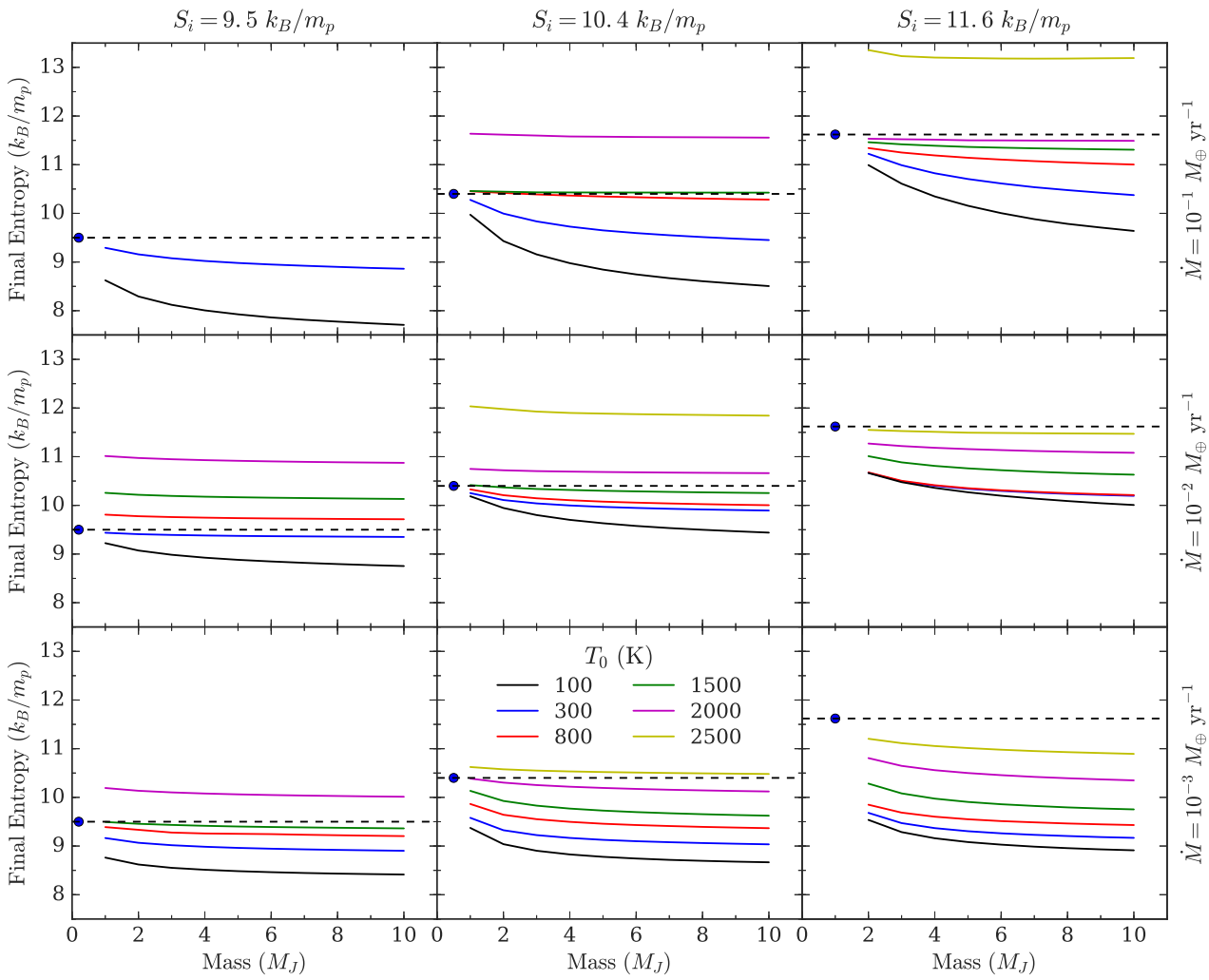

Figure 3.6: Final entropy as a function of mass for accretion models. Each panel shows a particular choice of $\dot{M}$ and S_i indicated by the labels along the top and right of the figure. The blue dots and dashed lines indicate the initial entropy and mass, which are (9.5, 0.2), (10.4, 0.5), and (11.6, 1.0) ($k_B/m_p, M_J$) from the left column to the right column. The lines correspond to accretion with different surface temperature T_0 (*see legend*). Not all temperatures are shown in some panels because of convergence issues at lower values of S_i and larger values of $\dot{M}$ or T_0.

avoids convergence issues that arise when changing from accreting to cooling surface boundary conditions at the end of accretion.

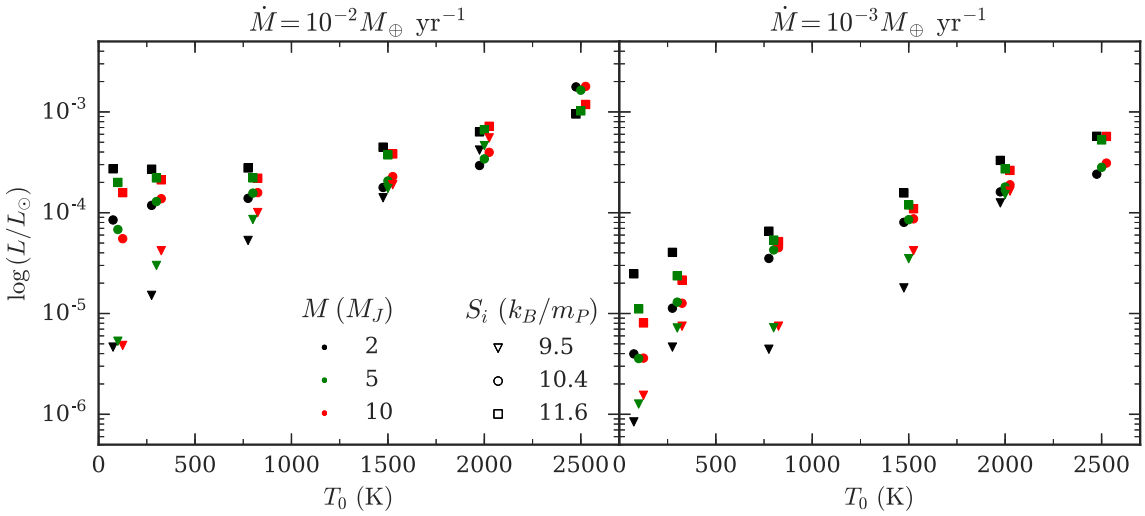

Figure 3.7: Luminosity at the onset of post-accretion cooling as a function of surface temperature during accretion for $\dot{M} = 10^{-2}\ M_\oplus\ yr^{-1}$ (*left panel*) or $\dot{M} = 10^{-3}\ M_\oplus\ yr^{-1}$ (*right panel*). The colors indicate the final planet mass, while the different symbols indicate the initial entropy of the object at the beginning of accretion (*see legend*). For visual clarity, the markers are given a temperature offset of −25, 0, and +25 K for a respective final mass of 2, 5, and 10 M_J.

Figure 3.7 shows that cold starts require that we choose the lowest values of boundary temperature $T_0 < 300$ K (comparable to typical nebula temperatures T_{neb}), accretion rate $\dot{M} = 10^{-3}\ M_\oplus$ yr^{-1}, and initial entropy $S_i = 9.5\ k_B/m_p$. In these cases we find luminosities that are comparable to and even lower than the cold-start luminosities of Marley et al. (2007), who found $2–3 \times 10^{-6}\ L_\odot$ for $M = 4–10\ M_J$ and $\approx 6 \times 10^{-6}\ L_\odot$ for $M = 2\ M_J$. However, increasing any of these parameters beyond these lowest values gives luminosities larger than Marley et al. (2007). For example, $\dot{M} = 10^{-2}\ M_\oplus$ yr^{-1} (the limiting accretion rate assumed by Marley et al. 2007) gives $L_p \gtrsim 5 \times 10^{-6}\ L_\odot$, even for $T_0 = 100$ K. Increasing T_0 beyond 300 K gives $L_p \gtrsim 5 \times 10^{-6}\ L_\odot$ even for $\dot{M} = 10^{-3}\ M_\oplus$ yr^{-1}.

Temperatures as low as $T_0 \sim T_{neb}$ are possible within the boundary prescription of Bodenheimer et al. (2000), in the case where the flow remains optically thin throughout the growth of the planet. However, the situation in the literature regarding the outer boundary conditions for cold accretion is some-

what confused. The boundary conditions often used in energy approaches to cold accretion, namely that $L \approx 4\pi R^2 \sigma T_{eff}^4$ and $P_0 = (2/3)(g/\kappa)$ (e.g. Hartmann et al. 1997; Mordasini 2013, see § 1.5), where T_{eff} is the effective temperature, i.e. the usual boundary conditions for a cooling planet, give temperatures significantly larger than T_{neb} and in our models these conditions do not lead to cold starts. The cooling time of the planet is generally longer than the accretion timescale (see figure 5 in Berardo et al. 2017), so that this cooling boundary condition leads to only a small change in entropy during accretion (see the difference between the horizontal solid and dashed lines in Fig. 3.3). Only by holding the boundary temperature to a low value are we able to drive a large enough luminosity to accelerate the cooling and reduce the internal entropy significantly on the accretion timescale.

However, as discussed in §1.5, shock models developed in the context of star formation (Stahler et al., 1980; Commerçon et al., 2011) and planet accretion (Marleau et al., 2017) suggest that the surface temperature is likely to be significantly larger than either of these prescriptions for cold starts. In these models, the gas at the surface of the planet is heated by some fraction of the accretion luminosity generated at the shock to a temperature T_{hot} given by $4\pi R^2 \sigma T_{hot}^4 \sim L_{accr} \approx GM\dot{M}/R$. In that case our results suggest that core accretion will produce hot starts, with high entropy $S_c \sim 12\ k_B/m_p$ set by S_{min} and luminosity $L_p \gtrsim 10^{-4}\ L_\odot$.

3.5 Comparison of cooling curves to data

The subsequent cooling of the planets is shown in Figure 3.8 and compared to measured luminosities of directly-imaged planets. We include those planetary-mass companions listed in Table 1 of Bowler (2016) that are consistent with a hot-start mass $\lesssim 10\ M_J$ (the maximum mass in our models) with ages $\lesssim 10^8$ yr, as well as the protoplanet HD 100546 b which has a bolometric luminosity given by Quanz et al. (2015). The four points numbered 5–8 refer to planetary companions orbiting at < 100 au, and so are perhaps most likely to have formed by core accretion. The cooling curves depend on both S_i and T_0 (which set the post-formation entropy), and the planet mass, so that determining the formation conditions is difficult

without an independent measurement of the planet mass (e.g. Marleau & Cumming 2014). Even then, Figure 3.8 shows that, at the age of these planets ($\approx$ 20–40 Myr), the variation in luminosity with shock temperature T_0 is less than a factor of a few and can be much smaller for low planet masses and hotter initial conditions. Younger planets (with ages ~ 10^6–10^7 yr) have a better memory of their post-formation state. However, of the other low-mass objects shown, 2M 0441 b and 2M 1207 b orbit brown dwarfs, and ROXs 42Bb and HD 106906 are both seen at wide separations (140 and 650 au respectively), so it is not clear whether they formed by core accretion. The remaining data points are HD 100546 b and 51 Eri b, both of which shall be discussed in the next chapter.

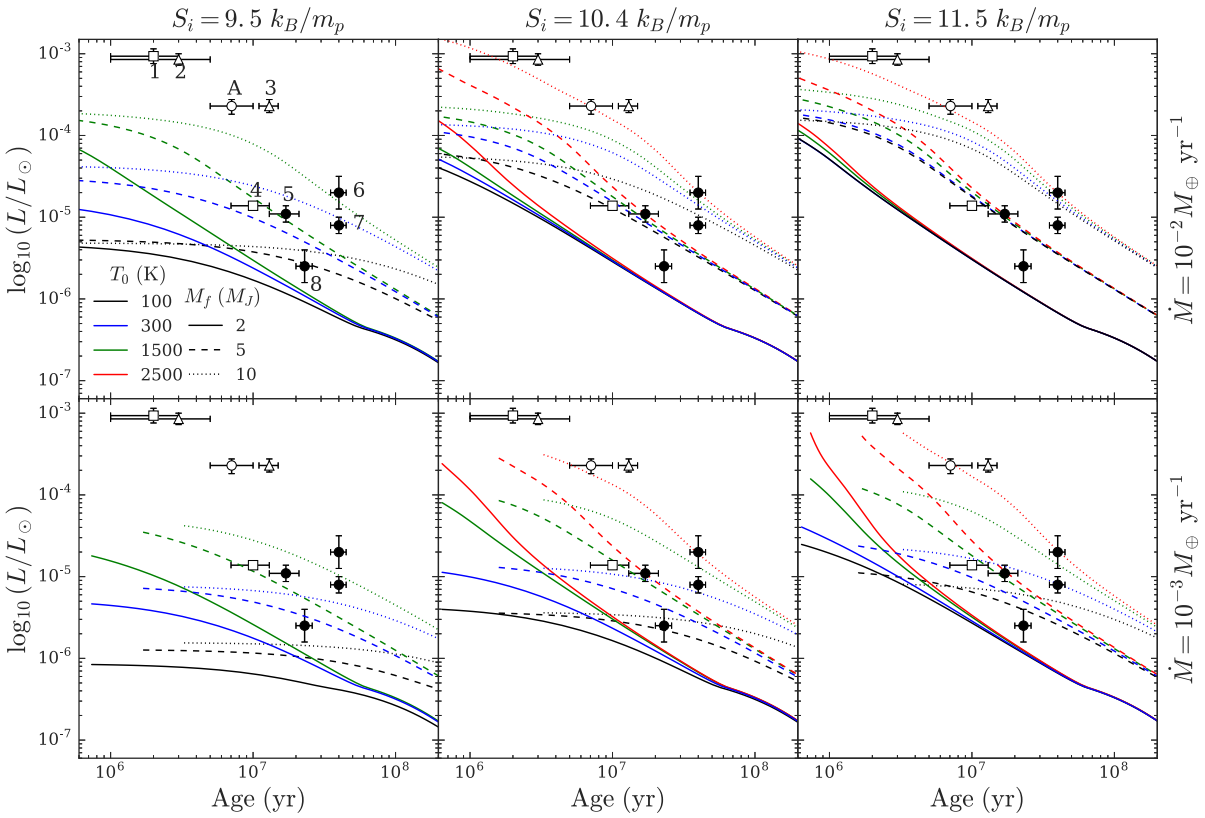

Figure 3.8: Post-accretion cooling compared with directly-imaged exoplanets. The curves show the evolution of the luminosity after accretion ends for final masses $M_f = 2, 5$, and $10\ M_J$ in MESA (*line style*) and surface temperature during accretion $T_0 = 100$–2500 K (*line color*). The entropy at the beginning of accretion (the accretion rate) is constant along columns (rows); see top (right) titles. Because these are post-accretion luminosities, the curves begin at different ages based on the total accretion time, which depends on $\dot{M}$ and the final mass. The data points are for objects with hot-start mass $\lesssim 10\ M_J$ from the compilation of Bowler (2016) as well as the protoplanet HD 100546 b, and use the age *of the host star*: **1**: ROXs 42B b (Currie et al., 2014a), **2**: 2M0441+2301B b (Todorov et al., 2014), **3**: HD 106906 b (Bailey et al., 2014), **4**: 2M1207 3932 b (Chauvin et al., 2004), **5**: HD 95086 b (Rameau et al., 2013), **6**: HR 8799 d (Marois et al., 2008), **7**: HR 8799 b (Marois et al., 2008), **8**: 51 Eri b (Macintosh et al., 2015), **A**: HD100546 b (Quanz et al., 2015). The symbol type indicates objects around brown dwarfs (*open squares*), objects at > 100 au (*open triangles*), planets at < 100 au orbiting stars (*closed circles*), and protoplanets (*open circle*).

4

Time Dependent Accretion Conditions

The models of the previous chapter in which the temperature T_0 at the boundary of the accretion shock is held constant are not likely to represent what is actually found in nature. It is much more likely that as the planet grows, the boundary conditions will change as well since quantities such as the ram pressure or the kinetic energy of the material (which is accreted in free-fall) are dependent on the mass and radius of the planet. This does not mean that the results of the previous section are without merit, as they allow an understanding of how the thermodynamic properties of accreted material will influence the formation of a planet. A shortfall of these models is that they lack predictive power when attempting to model the accretion history of an actual directly imaged exoplanet, which would have accreted under different conditions. In order for a such a thing to be done, we shall update our models by using a time-dependent temperature boundary condition.

4.1 The Accretion Shock

As discussed in § 1.3 (see figure 1.2), the accretion shock plays a key role in determining the properties of the accreted material by dictating the amount of energy that gets incorporated into the planet (Fortney et al., 2005). An understanding of how the excess energy (which is radiated away from the planet) interacts with the accretion flow is also required. In the case of an optically thin flow, the radiated energy will leave the system and can be ignored. However if the flow is optically thick, this energy will be re-absorbed by the stream of accreting material and be advected back into the shock region.

In the context of gas giant formation, the core accretion models of Pollack et al. (1996), Bodenheimer et al. (2000), and Hubickyj et al. (2005) are based on the assumption that the shock is isothermal, with a temperature set by integrating the radiative diffusion equation inwards through the spherical accretion flow from the nebula (i.e. the local circumstellar disk) to the shock. In the limit where the flow is optically thin, the shock temperature is then the nebula temperature, but could be much larger if the flow is optically thick (see discussion in § 2 of Bodenheimer et al. 2000). The cold accretion limit of these models is therefore that the post-shock temperature of the gas is $T_0 = T_{neb}$, or 150 K in the calculations of Hubickyj et al. (2005) (although whether the temperatures in the models corresponding to the Marley et al. 2007 cold starts were that low was not explicitly reported).

An alternative approach that has been used in a variety of contexts is to model the shock efficiency by the fraction of the specific accretion energy GM/R that is incorporated into the star or planet. This is implemented either by adding an amount $\eta GM/R$ to the specific internal energy of the accreted matter if following the detailed structure with a stellar evolution code (Prialnik & Livio 1985; Siess et al. 1997; Baraffe et al. 2009), or by adding a contribution $\eta GM\dot{M}/R$ to the planet's luminosity if following the global energetics (Hartmann et al. 1997). For gas giant accretion, Mordasini et al. (2012) and Mordasini (2013) step through sequences of detailed planet models in thermal steady state by tracking the global energetics, and model cold or hot accretion by not including or including the accretion luminosity in the internal luminosity of the planet. Owen & Menou (2016) recently applied the approach of Hartmann

et al. (1997) to disk-fed planetary growth, calculating η as set by the disk boundary layer.

In these approaches, the cold limit corresponds to setting $\eta = 0$, which means that the accreting material adjusts its temperature to match the gas already at the surface. With this boundary condition, the cooling history of the accreting object is affected by accretion only through the fact that its mass is growing, which changes its thermal timescale. Even for $\eta = 0$, the temperature at the surface can be much larger than T_{neb}, and so this is a different cold limit than in Bodenheimer et al. (2000). For example, taking a typical internal luminosity $L_{int} \sim 10^{-4}\ L_{\odot}$ and planet radius 2 R_J gives $T_0 = T_{therm} \approx (L_{int}/4\pi R^2\sigma)^{1/4} \approx 1300\ K$, where σ is the Stefan–Boltzmann constant.

In the hot limit with $\eta = 1$, the surface temperature is given by $T_0 = T_{hot} \approx (L_{accr}/4\pi R^2\sigma)^{1/4}$ where $L_{accr} \approx GM\dot{M}/R$ is the accretion luminosity which when scaled to typical values of $\dot{M}$, M, and R can be written as

$$L_{accr} \approx 4.4 \times 10^{-3}\ L_{\odot} \left(\frac{\dot{M}}{10^{-2}\ M_{\oplus}\ yr^{-1}}\right)\left(\frac{M}{M_J}\right)\left(\frac{R}{2\ R_J}\right)^{-1}. \quad (4.1)$$

Shock models suggest that the post-shock temperature is more likely to be close to T_{hot} than T_{neb}. Stahler et al. (1980) argued that, even if the accretion flow is optically thin, the outer layers of the protostar (or here the planet) will be heated because some of the energy released in the shock is radiated inwards (see fig. 5 of Stahler et al. 1980 and associated discussion; see also the discussion in Calvet & Gullbring 1998 and Commerçon et al. 2011). For an optically thin accretion flow, Stahler et al. (1980) derived the relation $4\pi R^2\sigma T^4 \approx (3/4)L_{accr}$ for the post-shock temperature (see their eq. [24]), which is $(3/4)^{1/4}T_{hot} \approx 3100\ K$. The factor of 3/4 relies on an approximate estimate of the outwards radiation that is reprocessed and travels back inwards towards the surface, but the temperature is only weakly affected (for example a factor 1/4 would still give 2300 K). This suggests that the temperature in the post-shock layers is $T_0 \gg T_{neb}$ and even $T_0 \gg T_{therm}$.

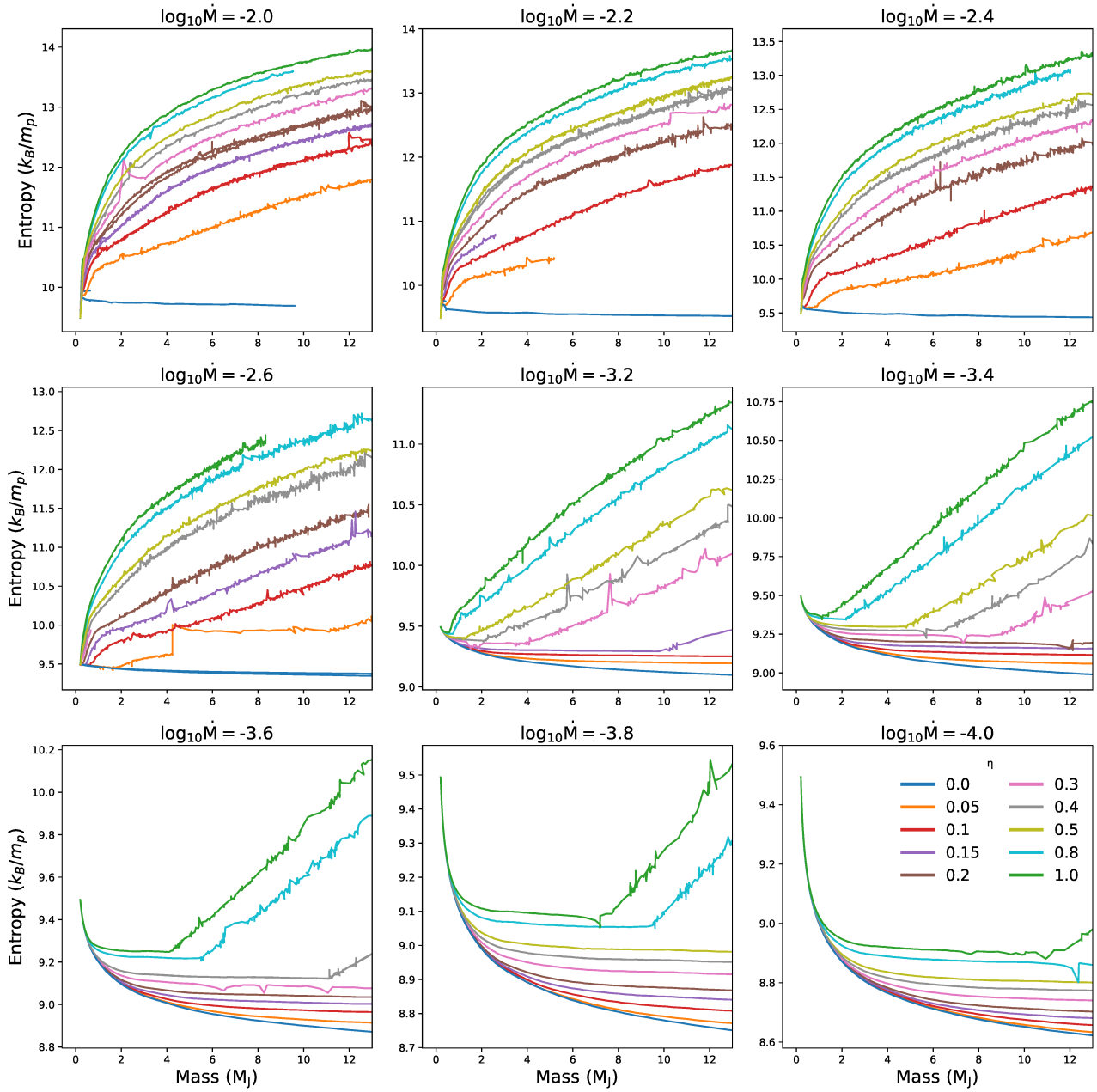

Figure 4.1: The internal entropy of a planet as it accretes from 0.5 $\mathrm{M_J}$ through to 15$\mathrm{M_J}$. Each panel corresponds to a different value for the accretion rate, which decreases from the top left to the bottom right. Within a panel, different curves correspond to different values of η which are shown in the legend in the bottom right panel. Note the differing scales for entropy for each panel.

4.2 MESA Accretion Models

In order to simulate accretion in MESA, we must make a choice for the outer boundary conditions. Since detailed calculations of the radiative transfer associated with the shock are in the early stages (e.g. Marleau et al. 2017), we shall continue the trend of modelling the efficiency of the accretion shock with a parameter $0 \leq \eta \leq 1$. We shall use this parameter to measure the amount of the accretion luminosity that gets incorporated into the planet through the surface temperature as:

$$T_0 = \left(\eta \frac{L_{accr}}{4\pi R^2 \sigma} + \frac{L_{int}}{4\pi R^2 \sigma} \right)^{\frac{1}{4}} \tag{4.2}$$

where $\eta = 0$ implies that all of the accretion luminosity has been re-radiated outwards (a perfectly efficient shock) and $\eta = 1$ implies that all of the luminosity has been incorporated into the planet (a completely inefficient shock). For the pressure P_0 we shall continue to use the ram pressure given by eq. [1.5]. Throughout a simulation, MESA will calculate the values of mass, radius, and the luminosity of the planet and so the input parameters which we are free to tune for a given simulation are the accretion rate $\dot{M}$ and the shock efficiency η. The accretion rate will be taken to vary between $10^{-2} - 10^{-4}\ M_\oplus\ \mathrm{yr}^{-1}$ between models, although it is held constant for a particular model.

We run a grid of accretion models in order to see how the final internal entropy of the planet is dependent upon these two parameters, and we show the results of this in figure 4.1. For these models, during a single simulation we record the internal entropy at various masses which allows the modelling of a planet with final masses from 1 $M_J$up to 13M_J, although some models become numerically divergent before this final mass. The shapes we see in these figures are the ubiquitous 'tuning-forks' shown comparing hot and cold start models such as in Marley et al. (2007) and Mordasini (2013). Some of the curves exhibit jitter or sharp changes due to numerical stability issues as MESA attempts to smoothly join the existing planet to the imposed boundary conditions, although in all cases this is over a small entropy range of $\lesssim 0.2\ \mathrm{k_B/m_p}$.

It is seen that for a given accretion rate, as η varies from 0 to 1, the models transition from cold-start

to hot-start. We may understand this in the context of the accretion regimes from the previous chapter, where here any curve which increases from its starting point is in the heating regime, and any curve which decreases is in the cooling/stalling regime. Only for very low values of $\eta \lesssim 0.2$ and $\dot{M} < 10^{-3} M_\oplus \text{ yr}^{-1}$ that a cold-start planet is produced, which is in agreement with the conclusions of the previous chapter. Indeed, many of the panels show only one branch of the tuning fork, such as for $\dot{M} = 10^{-2.2} M_\oplus \text{ yr}^{-1}$ where all models are heating except for $\eta = 0$. Additionally we see certain cases where the planet initially was cooling and then transitioned into heating, such as for $\eta = 1$ and $\dot{M} = 10^{-3.6} \text{ M}_\oplus \text{yr}^{-1}$. In the previous chapter, a planet would accrete in either the cooling, stalling, or heating regime exclusively. However since the accretion regime is dictated by boundary conditions which are now taken to be fully time dependent, we see planets which go through multiple regimes during accretion.

4.3 Calculating Cooling curves of accretion models

We shall use these models to estimate accretion parameters for two directly imaged exoplanets. The first is HD 100546 b, which is thought to be a protoplanet that is currently undergoing accretion in a circumstellar disk. The evidence for core accretion, along with its younger age of $\sim 5 \times 10^6$ yr, puts it in the range of planets that will be the most useful in understanding the properties of planets produced by core accretion. Additionally, as previously mentioned in § 1.4, it appears that the intrinsic luminosity of the planet can be distinguished from the fraction of the accretion luminosity which has not been absorbed, which is an important point to consider when discussing accreting objects. Figures 3.7 and 3.8 show that using the methods of the previous chapter, a luminosity of $> 10^{-4} L_\odot$ is obtained only for hot outer boundaries $T_0 \gtrsim 2000$ K or higher entropies at the onset of runaway accretion $S_i \gtrsim 10 \, k_B/m_p$.

The other planet of interest is 51 Eri b. With a bolometric luminosity of $1.6\text{–}4 \times 10^{-6} L_\odot$ (Macintosh et al., 2015), it is perhaps the most likely observed candidate for a cold start. Figure 3.8 shows that the mass of 51 Eri b could be 10 M_J if $T_0 = 100$ K, but even a small increase to $T_0 = 300$ K requires a lower mass $M \lesssim 3 \, M_J$. Therefore it seems likely that the mass of 51 Eri b is close to the hot-start mass, which we shall

further confirm in this chapter.

The two pieces of observational data which will be used are the estimated ages and luminosities of both planets. In order to compare the data to our models, we need to calculate cooling curves for all the accretion models that were made. It proved difficult in MESA to follow a single model completely from formation through to cooling, due to the sharp change in parameters when accretion is turned off. In order to alleviate this, we use the technique described in § 2.1. The mass and internal entropy of the planet are recorded at the end of accretion and then a new MESA simulation is set-up which does not include accretion effects, allowing the planet to cool.

We show a selection of these cooling curves in figure 4.2. Any given value of η and $\dot{M}$ will correspond to a single curve from one panel of figure 4.1. Along this curve at mass intervals of ~0.2 M_J the entropy is recorded, and a cooling curve is made. In this way, a single panel in figure 4.2 corresponds to a single curve in figure 4.1. In addition to these cooling curves, we also show the observational data for 51 Eri b and HD 100546. This figure illustrates several points about how the two free parameters influence formation. As expected, a higher value of η will lead to more luminous planets post accretion, since the planet retains a higher fraction of the accretion luminosity during formation. For the accretion rate, we note that it influences the evolution in two ways. First through the ram pressure, which in turn sets the surface entropy. As seen in Appendix A, the entropy depends inversely on the pressure, which by equation 1.5 depends linearly on $\dot{M}$. Thus a lower accretion rate would imply a higher value of surface entropy, leading to a higher luminosity. However the accretion rate also dictates the time-scale of accretion. As the accretion rate tends to zero, accretion effectively shuts off and the planet will just cool. In this way, a lower accretion rate allows the planet a chance to cool during accretion and so results in a lower luminosity (as is seen by comparing the top and bottom rows in figure 4.2.

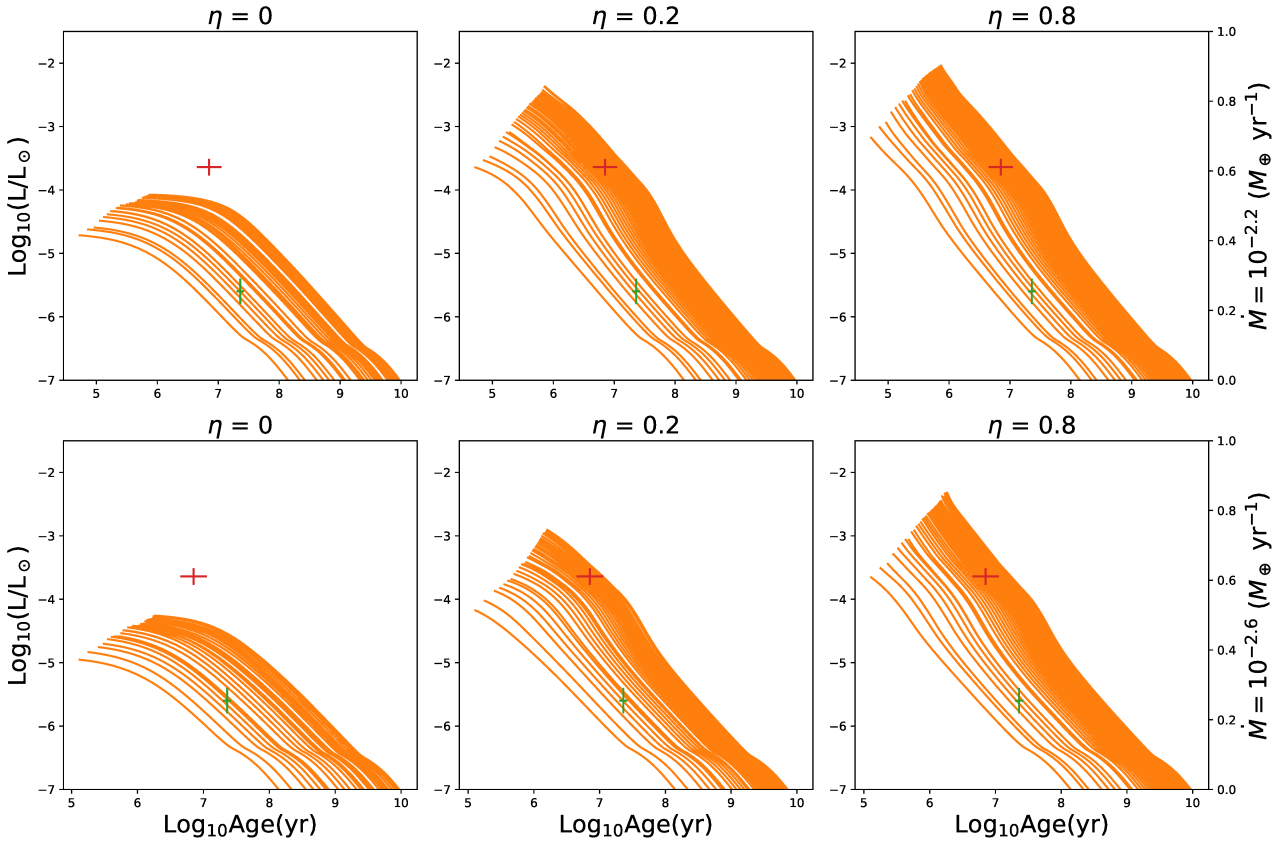

Figure 4.2: Cooling curves for core accretion models with varying values of η and $\dot{M}$, indicated along the top and right side of the panels. Within a panel, curves are shown for masses ranging from 1 M_J- 15 M_J(increasing from lower to higher luminosity). The red and green points show observational data for HD100546 and 51 Eri b.

4.4 Applying Models to 51 Eri b and HD 100546 b

One can see from figure 4.2 that choosing for example $\eta = 0$, it is impossible to make a model that agrees observationally with HD 100546 (for the mass range we consider). We attempt to quantify this statement in order to constrain the possible values of η and $\dot{M}$, as well as to calculate the mass likelihood function for the two planets based on our models. Assuming a uniform prior on the mass for both planets, and given their observed ages t_{actual} along with an error bar σ_t as well as an observed luminosity L_{actual} with corresponding error σ_L, the likelihood is calculated as

$$\text{Likelihood}(t, L) = \exp\left(-\left(\frac{t - t_{actual}}{2\sigma_t}\right)^2\right) \times \exp\left(-\left(\frac{L - L_{actual}}{2\sigma_L}\right)^2\right) \tag{4.3}$$

where in the above equation the luminosity L is the 3 dimensional function

$$L = L(\eta, \dot{M}, M) \tag{4.4}$$

which is calculated by MESA and t is the age of the planet.

This luminosity can be read off the corresponding cooling curve such as one seen in figure 4.2. The age used in the calculation of the likelihood is dealt with in a different manner. In reality, since the age of the planet comes from association with the host star, it is at best an upper limit. Due to this uncertainty, when calculating the value of a likelihood for a given choice of $(\eta, \dot{M}, M)$, we shall marginalize over the age by randomly sampling 100 ages with a Gaussian spread of width σ_t around the observed value. In figure 4.3 we show the calculated likelihoods for both 51 Eri b and HD 100546 for selected values of accretion rate, where the likelihood has been scaled so that the highest value is one.

For 51 Eri b, the likelihood has no dependence on the shock efficiency for accretion rates $\dot{M} \gtrsim 10^{-3}\ M_\oplus\ \text{yr}^{-1}$. The reason for this is that regardless of the value of η, all planets form with a sufficiently high luminosity such that they have joined on to their respective hot start cooling curve (defined by their mass) by the time they reach the age of 51 Eri b. Another way of saying this is that by the age of 51 Eri b, all traces of formation conditions have been removed, such that the value of η won't alter the estimated mass. This result is contrary to that of Marley et al. (2007), where high mass planets are formed with low enough luminosities to explain 51 Eri b. In our models this is only seen to some degree for the lowest value of accretion rate. For $\dot{M} = 10^{-4}\ M_\oplus\ \text{yr}^{-1}$, the likely mass range widens to $2 - 9\ M_J$ at $\eta = 0$, and in fact the mass range does increase between each panel as the accretion rate drops, although the effect is more subtle for higher accretion rates.

In the case of HD 100546 b, at an accretion rate of $\dot{M} \lesssim 10^{-2.6}\ M_\oplus\ \text{yr}^{-1}$ there is an increase in the mass

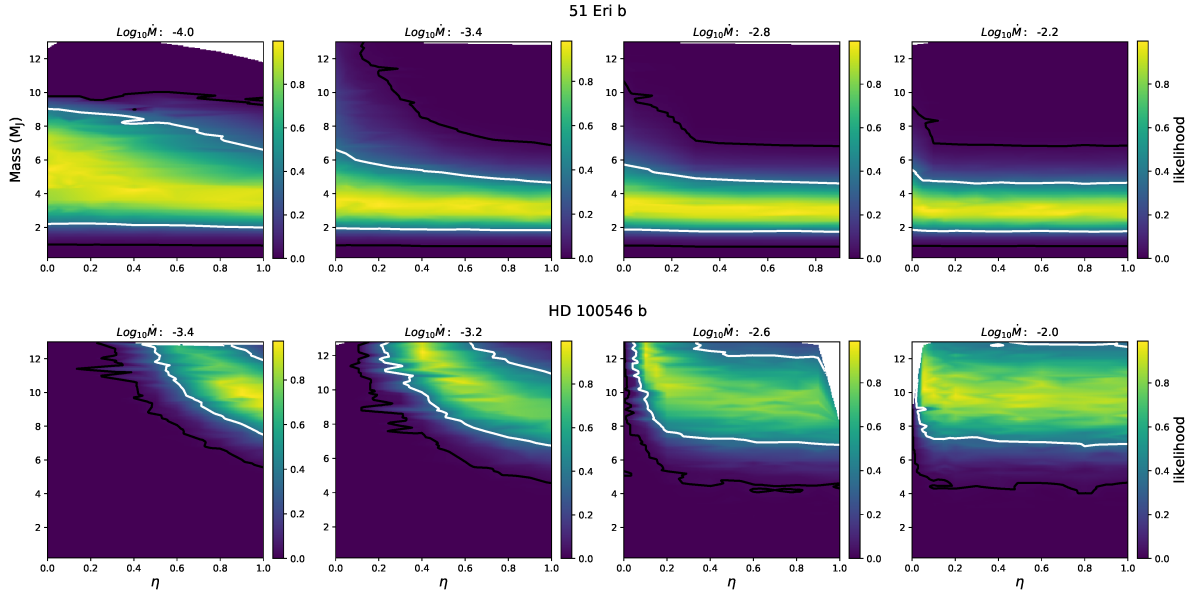

Figure 4.3: Heat maps showing scaled likelihoods calculated as a function of mass, accretion rate, and shock efficiency parameter for 51 Eri b (top row) and HD 100546 b (bottom row). Note the differing scales for the efficiency parameter (see text for discussion). The white and black lines show contours of one and two σ respectively.

for lower values of η, where the mass likelihood shifts upwards since for lower values of η, a higher mass is required to match the observed luminosity of HD 100546 b. However as with 51 Eri b, at high enough values of the accretion rate η has no effect on the likelihood, indicating again that all models produce planets which immediately join the hot start cooling track.

Due to the lack of a strong dependence on η, we now marginalize over it by calculating

$$\text{Likelihood}(\dot{M}, M) = \sum_{\eta} \text{Likelihood}(\dot{M}, M, \eta) \tag{4.5}$$

and show the results of this in figure 4.4. We see a similar trend for 51 Eri b, where there is a rise in possible mass only for the lowest accretion rates (which as mentioned facilitate cold starts). With regards to HD 100546 b, we see a sharp cutoff in accretion rate where the luminosity of the planets produced is too low to match observations. Note that this cutoff is very likely due to the cutoff in mass considered in our

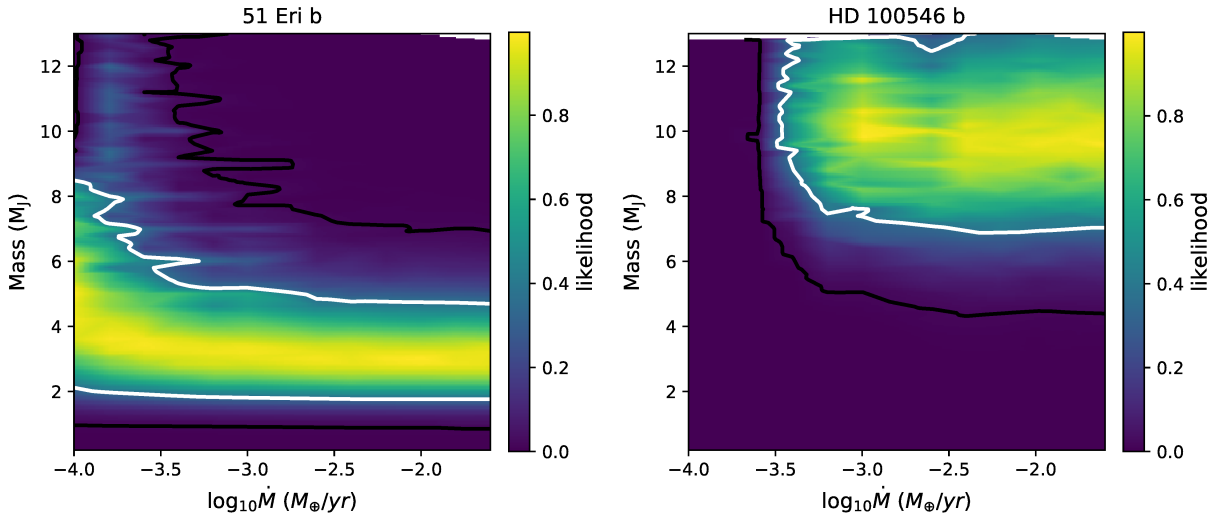

Figure 4.4: Heat maps showing the calculated likelihood for 51 Eri b (left panel) and HD 100546 b(right panel) after having marginalized over the accretion shock efficiency η.

models, and it is possible that a higher mass planet with M > 13 M_J could provide a sufficient luminosity.

We now marginalize over the accretion rate (in addition to η) in order to obtain the probability distributions for the masses of the two planets, the results of which are shown in figure 4.5. We once again see that based on our models, high masses for 51 Eri b are not likely. For comparison we plot the literature masses from table 1 of Bowler (2016), and while there appears to be a good agreement for HD 100546 b there is a discrepancy for 51 Eri b. A possible cause of this comes from the way the cooling curves were calculated. Recall that the cooling curve is calculated by accreting the planet up to a certain mass value, recording the internal entropy, and then creating a new, non-accreting model with the correct entropy and mass which is allowed to cool. If the cooling models were formed with a luminosity offset compared to the accreted model, this would translate to a mass offset in the likelihood, since the cooling curve for a given mass would appear to be that of a higher/lower mass. We show one example of this in figure 4.6, comparing the final luminosities of the accretion models with the initial luminosities of the cooling mod-

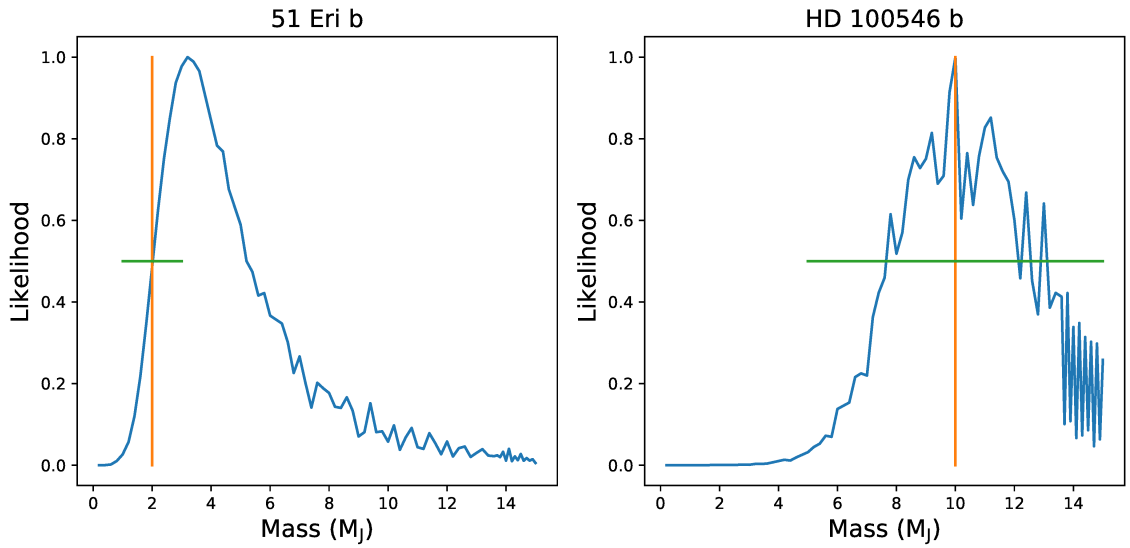

Figure 4.5: Mass likelihoods for 51 Eri b (left panel) and HD 100546 b(right panel) after having marginalized over both the accretion shock efficiency η and the accretion rate $\dot{M}$. The orange line shows the literature value for the masses, and the green line shows the error bar on the mass.

els. While there is a minor shift in luminosity, this is to be expected since the hot outer boundary of the planet will quickly cool post accretion. Furthermore, we see an offset at high masses as well, although our model predicts the correct mass for HD 100546 b, so this minor luminosity offset is not likely to be the cause of the mass offset. Nonetheless, we may conclude that a low mass (corresponding to a hot start) is the most likely scenario for 51 Eri b.

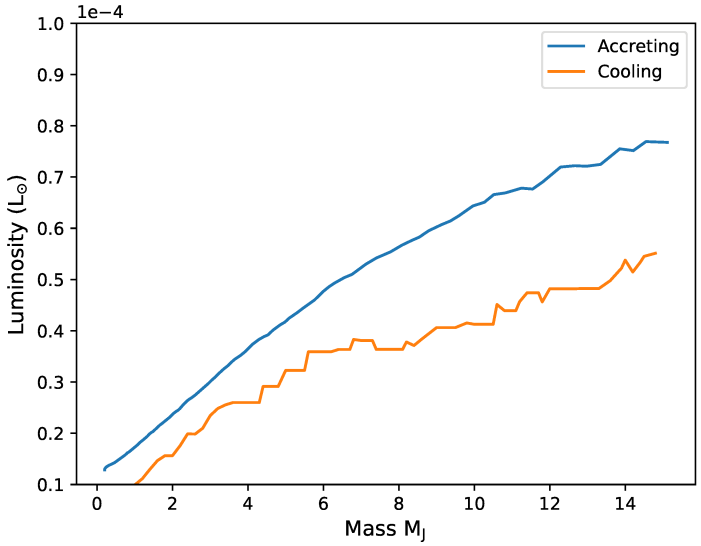

Figure 4.6: Comparison between the luminosity of models at the end of accretion (blue line) and at the beginning of cooling (orange line) after a new MESA model has been made.

5

Conclusion

The primary goal of this work has been to describe the physics of core accretion in greater detail than has been done in the past. We have attempted to quantify the conditions required for both hot and cold start models in order to estimate the likelihood of one versus the other, and we now provide an overview of our results.

5.1 The Accretion Process

We have first shown that the choice of boundary conditions T_0 and P_0 during core accretion leads to three different accretion regimes (§ 3.2 and Fig. 3.2), which depends on the difference between the entropy of the material deposited by the accretion shock $S_0(T_0, P_0)$ and the initial internal entropy S_i:

- The *cooling regime*. For $S_0 \lesssim S_i$, the planet becomes fully convective, and the superadiabatic gradient drives a large luminosity that leads to rapid cooling. The cooling luminosity is sensitive to

the boundary pressure P_0, with larger P_0 leading to faster cooling. If the cooling is rapid enough compared to the accretion timescale, the end state of this regime is that the internal entropy becomes equal to the surface entropy $S_f \approx S_0$. This regime occurs for low boundary temperatures $T_0 \lesssim 500\text{–}1000\ K$.

- The *stalling regime*. For $S_0 \gtrsim S_i$, the entropy decreases inwards in a radiative envelope. Provided the entropy contrast is not too great, the envelope joins smoothly onto the interior convection zone. The hot envelope causes the radiative-convective boundary (RCB) to lie at higher pressure than in an isolated cooling planet with the same internal entropy, lowering the luminosity at the RCB and slowing the cooling. In this regime, the final entropy lies close to the initial value of entropy at the onset of accretion $S_f \lesssim S_i$, depending on how much the cooling is slowed. This regime occurs at intermediate temperatures $T_0 \approx 1000\text{–}2000\ K$.

- The *heating regime*. For boundary temperatures $T_0 \gtrsim 2000\ K$, the entropy difference $\Delta S = S_0 - S_i$ cannot be accommodated by the radiative envelope. Instead, the entropy decreases inwards through the envelope to a value $S_{min} > S_i$ and a second convection zone with entropy S_{min} accumulates above the original convective core.

Furthermore, we have shown that the luminosity of a young gas giant formed by core accretion depends not only on the outer boundary conditions (e.g. the shock temperature T_0) and accretion rate, but also the initial entropy S_i when runaway accretion begins, since it determines whether accretion occurs in the cooling, stalling, or heating regimes. Therefore the thermal state of the young planet in principle provides a link to the structure of the accreting core soon after the crossover mass is reached. This point was also made by Mordasini (2013), who found that the final entropy depended sensitively on the core mass because it sets the entropy of the envelope at detachment. We see here that for a wide range of intermediate temperatures for which accretion is in the stalling regime ($T_0 \approx 1000\text{–}2000\ K$, see Fig. 3.5), the final entropy is close to the entropy at the start of runaway accretion.

In chapter 4, using a more specific form of the outer boundary conditions (i.e. time dependent temperature) it was also shown that a high mass $\gtrsim 6\ M_J$ may be ruled out for 51 Eri b. When considering a model which tracks the accretion luminosity by considering the efficiency of the accretion shock it is found that, excluding very low accretion rates, high mass planets cannot be formed with a low enough luminosity to explain the observations of 51 Eri b. The collective results of this work suggest that only the most extreme boundary conditions (low T_0) can produce traditional cold start planets, and that such extreme conditions themselves are difficult to produce. The implications of this is that hot-start models are appropriate to use when attempting to estimate the mass of a directly imaged exoplanet, and the issue of degeneracy between mass and luminosity through cold-starts is not an issue.

5.2 Future Work

The focus of this work has been on understanding the internal entropy and luminosity of a core-accretion planet, with little regard to the details of the internal structure of the planet. For models in which the surface temperature is held constant, it was seen that for heating models an outer convective zone made up of the hotter accreted material forms above the initial, lower-entropy core. One may ask about the internal structure of a planet in the case where the surface temperature is changing over time, particularly a case where it increases during the evolution. As the planet gets more massive and contracts gravitationally, the accretion luminosity which goes like $L_{acc} \sim M/R$ will increase over time, implying a larger and larger T_0. Preliminary results not shown here suggest that in such a case instead of a sharp jump in internal entropy, the entropy profile gradually increases towards the surface of the planet. The interior of the planet is thus no longer convective, which has implications regarding the distribution of heavy elements within the planet (Leconte & Chabrier, 2012; Helled & Stevenson, 2017). The Ledoux criterion for convection, discussed in § 2.2, includes a term for compositional gradients when calculating the convective instability. It is thus possible that a non-homogeneous composition could shut down convection, which would alter the luminosity of the planet. This would delay the cooling of the planet, changing the shape of the cooling

curve and requiring further study in order to assign observed luminosities and ages to mass values. As an example, the observed luminosity of Saturn is larger than models currently predict (Pollack et al., 1977). If an inhomogeneous composition were present which altered Saturn's cooling, this could help explain the observed discrepancy.

One of the other goals of this work has been to develop MESA as a tool to study planet formation; we make our `inlist` and `run_star_extras` files available at http://cococubed.asu.edu/mesa_market/add-ons.html. It would be interesting to explore further modelling of gas giant formation in MESA, and overcome some of the limitations of our models. This will require taking into account energy deposition by planetesimals (see review in § 5.7 of Mordasini et al., 2015), modelling the contribution of dust grains to the envelope opacity (e.g. Ormel 2014; Mordasini et al. 2014), including possible composition effects on convection (e.g. Nettelmann et al. 2015), and extending to lower masses than considered here (see Chen & Rogers 2016).

A

The entropy in the envelope

This appendix has been taken from Berardo et al. (2017), written by the author and reproduced here with the permission of both co-authors A. Cumming and G.-D. Marleau.

In this appendix we calculate the entropy in the envelope of gas giants where it is a good approximation to assume an ideal gas consisting of molecular and atomic hydrogen as well as helium. In this case we can derive a simple formula for the entropy as a function of pressure and temperature. The ideal gas equation of state is $P = \rho k_B T/\mu m_p$ where the mean molecular weight μ is given by

$$\mu^{-1} = \frac{1 - Y}{1 + \chi_{H_2}} + \frac{Y}{4},$$

the molecular fraction $\chi_{H_2} = n_{H_2}/(n_{H_2} + n_H)$ (i.e. $\chi_{H_2} = 1$ (0) is purely molecular (atomic) hydrogen), and Y is the helium mass fraction. The number densities of H and H_2 can be computed from the Saha

equation

$$\frac{n_{H_2}}{(n_H)^2} = \frac{n_{Q,H_2} z_r}{(n_{Q,H})^2} e^{\Delta\epsilon/k_B T} \tag{A.1}$$

where $n_{Q,i} = (2\pi\mu_i m_p k_B T)^{3/2}/h^3$ and $m_p\mu_i$ is the mass of species i. We also consider that for hydrogen gas $n_{H_2} + n_H = P/k_B T$. The ionization energy $\Delta\epsilon$ is 4.48 $eV = 7.24 \times 10^{-12}$ erg (Blanksby & Ellison, 2003) and the rotational partition function for H_2 is given by

$$z_r = \frac{1}{2}\sum_{l=0}^{\infty}(2l+1)e^{-l(l+1)\Theta_{rot}/T}, \tag{A.2}$$

which in the limit of $T \gg \Theta_{rot}$ can be approximated as $z_r = T/(2\Theta_{rot})$, where $\Theta_{rot} = 85.4$ K (Hill, 1986). The pressure at which a given value of χ_{H_2} is reached at temperature T is

$$P\left(\chi_{H_2}, T\right) = 1.6 \times 10^6\ erg\ cm^{-3}\ \frac{\chi_{H_2}}{(1-\chi_{H_2})^2} T^{3/2} \exp\left(-\frac{5.4 \times 10^4\ K}{T}\right). \tag{A.3}$$

Contours of χ_{H_2} in the temperature–pressure plane are shown in Figure A.1. For $T \lesssim 2000\ K$ the envelope (pressure range $\approx 10^3$–$10^8\ erg\ cm^{-3}$) is molecular, but for higher temperatures atomic hydrogen must be included.

The entropy per particle of hydrogen and helium is

$$\frac{s_{H_2}}{k_B} = \frac{7}{2} + \ln\left(\frac{n_{Q,H_2}}{n_{H_2}}\right) + \ln\left(\frac{T}{2\Theta_{rot}}\right) \tag{A.4}$$

$$\frac{s_i}{k_B} = \frac{5}{2} + \ln\left(\frac{n_{Q,i}}{n_i}\right), \quad i = H, He. \tag{A.5}$$

We use the fact that the temperature is low enough so that the vibrational degrees of freedom of molecular hydrogen, which has a vibrational temperature $\Theta_{vib} = 6210$ K (Hill, 1986), are not excited. The entropy

per baryon $S_i = s_i/\mu_i$ is then

$$S_{H_2}/k_B = \frac{1}{2}\left(20.8 + \frac{5}{2}\ln T_3 - \ln \rho_{-5}\right), \tag{A.6}$$

$$S_H/k_B = \left(16.3 + \frac{3}{2}\ln T_3 - \ln \rho_{-5}\right), \tag{A.7}$$

$$S_{He}/k_B = \frac{1}{4}\left(19.8 + \frac{3}{2}\ln T_3 - \ln \rho_{-5}\right), \tag{A.8}$$

where $T_3 \equiv T/1000$ K and $\rho_{-5} \equiv \rho/(10^{-5}\ g\ cm^{-3})$. The total entropy per baryon is

$$S/k_B = \frac{(1-Y)}{(1+\chi_{H_2})}\left[2\chi_{H_2}S_{H_2} + (1-\chi_{H_2})S_H\right] + YS_{He} + S_{mix} \tag{A.9}$$

where S_{mix} is the entropy of mixing (Saumon et al., 1995) given by

$$S_{mix} = \frac{1}{\mu}\left(-x_H \ln x_H - x_{H_2}\ln x_{H_2} - x_{He}\ln x_{He}\right) \tag{A.10}$$

and the number fractions are

$$x_H = \frac{(1-Y)(1-\chi_{H_2})}{(1+\chi_{H_2})}\mu, \quad x_{H_2} = \frac{(1-Y)(2\chi_{H_2})}{(1+\chi_{H_2})}\frac{\mu}{2}, \quad x_{He} = Y\frac{\mu}{4}. \tag{A.11}$$

Considering the limit of purely molecular hydrogen ($\chi_{H_2} = 1$) we find $\mu = 2.28$, $S_{mix} = 0.18$ and the entropy is given by

$$\frac{S}{k_B/m_p} = 8.80 + 3.38\log_{10} T_3 - 1.01\log_{10}\left(\frac{P}{10^6\ erg\ cm^{-3}}\right), \tag{A.12}$$

having used the ideal gas equation of state to rewrite the density in terms of the temperature and pressure.

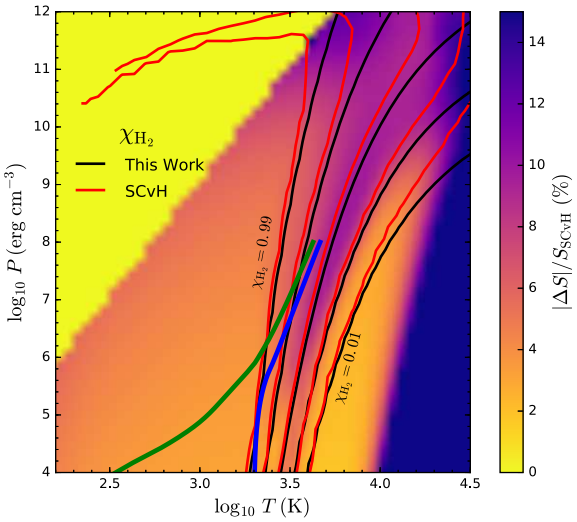

Figure A.1: Comparison between the entropy calculated using equation (A.9) and that of Saumon et al. (1995), $S_{\rm SCvH}$. The black and red lines indicate values of constant $\chi_{H_2}(P, T)$ obtained using equation (A.1) and from Saumon et al. (1995), respectively, for $\chi_{H_2} = 0.01, 0.1, 0.5, 0.9, 0.99$. The thick blue and green lines show envelope models from Figure 2 of Berardo et al. (2017) with surface temperatures of 2000 K and 150 K respectively. There is no SCvH entropy data in the upper-left, yellow region.

In the other limit of purely atomic hydrogen ($\chi_{H_2} = 0$) we find $\mu = 1.23$, $S_{mix} = 0.22$ and

$$\frac{S}{k_B/m_p} = 13.47 + 4.68 \log_{10} T_3 - 1.87 \log_{10} \left(\frac{P}{10^6\ erg\ cm^{-3}} \right). \tag{A.13}$$

From equations (A.12) & (A.13) we can read off the adiabatic index $\nabla_{ad} = (\partial \ln T/\partial \ln P)_S = 0.30$ for the molecular case and $\nabla_{ad} = 0.40$ for the atomic case.

In Figure A.1 we see how the results of the above equations compare to the values found in Saumon et al. (1995) (SCvH). The blue and green curves, which show envelope models calculated in § 3.2 of Berardo et al. (2017), are mostly in a region where the deviation from SCvH is only $|\Delta S|/S_{SCvH} \approx 2$–$5\%$. However, further into the envelope at higher pressures, the error increases to $\sim 10\%$ and so the more detailed equation of state tables from SCvH are required. Large deviations are seen for $T \gtrsim 10^4\ K$, where atomic hydrogen is ionized, but this region is not relevant for our envelope models. At lower temperatures, the largest deviations from SCvH occur where χ_{H_2} is transitioning from 0 to 1. Even though our calculation

of χ_{H_2} agrees well with that of SCvH (black and red contours in Fig. A.1), the small differences in χ_{H_2} are amplified in the total entropy because atomic hydrogen gives a much larger contribution to entropy than molecular.

B

Derivation of Convective Instability Criterion

In this appendix we derive the Schwarzschild criterion for convection in terms of temperature and pressure gradients. We then show how it may be re-written as an entropy derivative.

B.1 Schwarzschild Criterion

By following the discussion of § 10.4 of Carroll & Ostlie (2007), we observe what happens to a fluid element that is displaced from its surroundings adiabatically by an amount δr. Initially the fluid element is in thermal equilibrium with its surroundings, and is transported slowly enough so that it remains in pressure equilibrium but quickly enough that it does not remain in temperature equilibrium. In order for a fluid to be unstable to convection, a fluid parcel which is displaced upward must have a lower density than the surrounding gas (so that it continues to rise) which for small radial perturbations can be written as

$$\rho_{p_f} = \rho_i + \left.\frac{d\rho}{dr}\right|^{(p)} dr < \rho_i + \left.\frac{d\rho}{dr}\right|^{(s)} dr = \rho_{s_f} \tag{B.1}$$

where p and s refer to the parcel and surroundings, and f and i refer to final and initial quantities. Since initially the densities are equal, this can more succinctly be written as

$$\left.\frac{d\rho}{dr}\right|^{(p)} < \left.\frac{d\rho}{dr}\right|^{(s)} \tag{B.2}$$

and we assume an ideal gas with constant composition which allows us to write

$$\frac{d\rho}{dr} = \frac{d}{dr}\left(\frac{\mu m_u P}{k_B T}\right) = \frac{\rho}{P}\frac{dP}{dr} - \frac{\rho}{T}\frac{dT}{dr} \tag{B.3}$$

which we substitute both of back in to equation B.2

$$\left(\frac{\rho}{P}\frac{dP}{dr} - \frac{\rho}{T}\frac{dT}{dr}\right)\Big|^{ad} < \left(\frac{\rho}{P}\frac{dP}{dr} - \frac{\rho}{T}\frac{dT}{dr}\right)\Big|^{acd} \tag{B.4}$$

with the 'act' referring to the true temperature derivative and 'ad' referring to derivatives for the parcel, which is transported adiabatically. We may cancel out the pressure derivatives since the parcel is always in pressure equilibrium with the surroundings and use hydrostatic equilibrium (eq. [2.5]) to convert the radial derivative to a pressure derivative, which carries with it a negative sign

$$\left.\frac{P}{T}\frac{dT}{dP}\right|^{ad} < \left.\frac{P}{T}\frac{dT}{dP}\right|^{act} \tag{B.5}$$

Finally, recalling the definition of $\nabla = \frac{dlnT}{dln\rho}$ and dropping the 'act' subscript this can be written as

$$\nabla > \nabla_{ad} \tag{B.6}$$

which at last provides the criteria for determining if the fluid will be unstable to convection.

B.2 Entropy formulation of Schwarzschild Criterion

We now consider the radial entropy derivative within the planet $\frac{dS}{dr}$ which we may write as

$$\frac{dS}{dr} = \left(\frac{\partial S}{\partial T}\right)_P \frac{dT}{dr} + \left(\frac{\partial S}{\partial P}\right)_T \frac{dP}{dr} \tag{B.7}$$

and we shall rewrite the partial derivative $\frac{\partial S}{\partial P}$ using the triple product rule

$$\left(\frac{\partial S}{\partial P}\right)_T = -\left(\frac{\partial S}{\partial T}\right)_P \left(\frac{\partial T}{\partial P}\right)_S \tag{B.8}$$

which we substitute into equation B.7 to write

$$\frac{dS}{dr} = \left(\frac{\partial S}{\partial T}\right)_P \left[\frac{dT}{dr} - \left(\frac{\partial T}{\partial P}\right)_S \frac{dP}{dr}\right] \tag{B.9}$$

and for the temperature derivative in the above equation we write

$$\frac{dT}{dr} = \left(\frac{\partial T}{\partial P}\right)_{star} \frac{dP}{dr} \tag{B.10}$$

where 'star' denotes the actual gradient in the star/planet. This is substituted back into equation B.9 to give

$$\frac{dS}{dr} = \frac{T}{P}\left(\frac{\partial S}{\partial T}\right)_P \left[\frac{P}{T}\left(\frac{\partial T}{\partial P}\right)_{star} - \frac{P}{T}\left(\frac{\partial T}{\partial P}\right)_S\right] \frac{dP}{dr} \tag{B.11}$$

this can first be simplified by recognizing the heat capacity $C = T\frac{\partial S}{\partial T}$ and $\nabla = \frac{P}{T}\frac{\partial T}{\partial P}$ (where the second set of derivatives is at constant entropy, i.e. adiabatic) giving

$$\frac{dS}{dr} = \frac{C}{P}\left(\nabla - \nabla_{ad}\right) \frac{dP}{dr} \tag{B.12}$$

We now observe that the entropy gradient is a product of the pressure gradient which is negative (pressure

decreases radially outward from the planet) $\frac{dP}{dr} < 0$, the heat capacity C and the pressure P which are both positive. Finally, the Schwarzchild criterion is the statement that $\nabla > \nabla_{ad}$ and so we arrive at the conclusion that an equivalent description of convective instability is

$$\frac{dS}{dr} < 0 \tag{B.13}$$

C

MESA Code

In this appendix, we present the code found in the 'run_star_extras' file in MESA, which is used to set custom boundary conditions for temperature and pressure during accretion. The full directory of all MESA code used to construct the models can be found at http://cococubed.asu.edu/mesa_market/add-ons.html

```
subroutine shock_other_atm( &

        id, M, R, L, X, Z, kap, Teff, &
        lnT, dlnT_dL, dlnT_dlnR, dlnT_dlnM, dlnT_dlnkap, &
        lnP, dlnP_dL, dlnP_dlnR, dlnP_dlnM, dlnP_dlnkap, &
        which_atm_option, switch_to_grey_as_backup, ierr)

    {...}
```

```
! The values for Tflag and Pflag determine which set of boundary conditions
    to use for temperature and pressure at the photosphere
SELECT CASE(Tflag)
   CASE(1)
     !constant surface temp
     Teff = 900 !set value for constant surface temperature here
     lnT = log(Teff)
     dlnT_dL = 0
     dlnT_dlnR = 0
     dlnT_dlnM = 0
     dlnT_dlnkap = 0
   CASE(2)
     ! luminosity temp
     Teff=(L/(4*pi*R**2*sigma))**(1./4)
     lnT=log(Teff)
     dlnT_dL=Teff**(-4)/(16*pi*R**2*sigma)
     !dlnT_dlnR=-Teff**(-4)/(8*pi*sigma*R**2)
     dlnT_dlnR = -0.5
     dlnT_dlnM=0
     dlnT_dlnkap=0
    CASE(3)
     !shock temp, from eq. 32 in Stahler 1980, which considers the thermal
        equilibrium between
     !the shock, the incoming material, and the planetary luminosity
     Teff = (3*c_grav*M*mdot/(16*pi*sigma*R**3))**(1./4)
     lnT=log(Teff)
```

```
      dlnT_dL = 0
      dlnT_dlnR = -0.75
      dlnT_dlnM = 0.25
      dlnT_dlnkap = 0
     CASE(5)
      !Planet + accretion luminosity
      Teff=((L + (c_grav*M*mdot)/R)/(4*pi*R**2*sigma))**(1./4)
      lnT=log(Teff)
      dlnT_dL=Teff**(-4)/(16*pi*R**2*sigma)
      dlnT_dlnR = -0.75 + Teff**(-4)*L/(16*pi*R**2*sigma)
      dlnT_dlnM=Teff**(-4)*(c_grav*M*mdot)/(16*pi*R**3*sigma)
      dlnT_dlnkap=0
END SELECT
SELECT CASE(Pflag)
   CASE(1)
     !ram plus photospheric pressure
     lnP = log(mdot/(4*pi*R**2)*(2*c_grav*M/R)**(1./2) +
         (2.0/3.0)*(grav)/kap)
     dlnP_dL = 0
     dlnP_dlnR = -2.5-(1.0/3.0)*(grav/kap)*(1/EXP(lnP))
     dlnP_dlnM = 0.5+(1.0/3.0)*(grav/kap)*(1/EXP(lnP))
     dlnP_dlnkap = -(2.0/3.0)*(grav/kap)*(1/EXP(lnP))
   CASE(2)
     !only photospheric pressure
     lnP=log((2.0/3.0)*(grav)/kap)
     dlnP_dL=0
     dlnP_dlnR= -2.0
```

```
            dlnP_dlnM= 1.0
            dlnP_dlnkap=-1.0
          CASE(3)
            !ram only, obviously never used post accretion
            lnP = log(mdot/(4*pi*R**2)*(2*c_grav*M/R)**(1./2))
            dlnP_dL = 0
            dlnP_dlnR = -2.5
            dlnP_dlnM = 0.5
            dlnP_dlnkap = 0
        END SELECT
end subroutine shock_other_atm
```

References

Arras, P. & Bildsten, L. (2006). Thermal Structure and Radius Evolution of Irradiated Gas Giant Planets. , 650, 394–407.

Bailes, M., Bates, S. D., Bhalerao, V., Bhat, N. D. R., Burgay, M., Burke-Spolaor, S., D'Amico, N., Johnston, S., Keith, M. J., Kramer, M., Kulkarni, S. R., Levin, L., Lyne, A. G., Milia, S., Possenti, A., Spitler, L., Stappers, B., & van Straten, W. (2011). Transformation of a Star into a Planet in a Millisecond Pulsar Binary. *Science*, 333, 1717.

Bailey, V., Meshkat, T., Reiter, M., Morzinski, K., Males, J., Su, K. Y. L., Hinz, P. M., Kenworthy, M., Stark, D., Mamajek, E., Briguglio, R., Close, L. M., Follette, K. B., Puglisi, A., Rodigas, T., Weinberger, A. J., & Xompero, M. (2014). HD 106906 b: A Planetary-mass Companion Outside a Massive Debris Disk. , 780, L4.

Baraffe, I., Chabrier, G., Barman, T. S., Allard, F., & Hauschildt, P. H. (2003). Evolutionary models for cool brown dwarfs and extrasolar giant planets. The case of HD 209458. , 402, 701–712.

Baraffe, I., Chabrier, G., & Gallardo, J. (2009). Episodic Accretion at Early Stages of Evolution of Low-Mass Stars and Brown Dwarfs: A Solution for the Observed Luminosity Spread in H-R Diagrams? , 702, L27–L31.

Barclay, T., Rowe, J. F., Lissauer, J. J., Huber, D., Fressin, F., Howell, S. B., Bryson, S. T., Chaplin, W. J., Désert, J.-M., Lopez, E. D., Marcy, G. W., Mullally, F., Ragozzine, D., Torres, G., Adams, E. R., Agol, E., Barrado, D., Basu, S., Bedding, T. R., Buchhave, L. A., Charbonneau, D., Christiansen,

J. L., Christensen-Dalsgaard, J., Ciardi, D., Cochran, W. D., Dupree, A. K., Elsworth, Y., Everett, M., Fischer, D. A., Ford, E. B., Fortney, J. J., Geary, J. C., Haas, M. R., Handberg, R., Hekker, S., Henze, C. E., Horch, E., Howard, A. W., Hunter, R. C., Isaacson, H., Jenkins, J. M., Karoff, C., Kawaler, S. D., Kjeldsen, H., Klaus, T. C., Latham, D. W., Li, J., Lillo-Box, J., Lund, M. N., Lundkvist, M., Metcalfe, T. S., Miglio, A., Morris, R. L., Quintana, E. V., Stello, D., Smith, J. C., Still, M., & Thompson, S. E. (2013). A sub-Mercury-sized exoplanet. , 494, 452–454.

Berardo, D., Cumming, A., & Marleau, G.-D. (2017). The Evolution of Gas Giant Entropy During Formation by Runaway Accretion. , 834, 149.

Blanksby, J. S. & Ellison, B. G. (2003). Bond Dissociation Energies of Organic Molecules. *Acc. Chem. Res.*, 36(3), 255–263.

Bodenheimer, P., Hubickyj, O., & Lissauer, J. J. (2000). Models of the in Situ Formation of Detected Extrasolar Giant Planets. , 143, 2–14.

Bodenheimer, P. & Pollack, J. B. (1986). Calculations of the accretion and evolution of giant planets: The effects of solid cores. *Icarus*, 67(3), 391 – 408.

Bonnefoy, M., Boccaletti, A., Lagrange, A.-M., Allard, F., Mordasini, C., Beust, H., Chauvin, G., Girard, J. H. V., Homeier, D., Apai, D., Lacour, S., & Rouan, D. (2013). The near-infrared spectral energy distribution of β Pictoris b. , 555, A107.

Bowler, B. P. (2016). Imaging Extrasolar Giant Planets. , 128(10), 102001.

Bowler, B. P., Liu, M. C., Shkolnik, E. L., & Dupuy, T. J. (2013). Planets around Low-mass Stars. III. A Young Dusty L Dwarf Companion at the Deuterium-burning Limit. , 774, 55.

Burrows, A., Marley, M., Hubbard, W. B., Lunine, J. I., Guillot, T., Saumon, D., Freedman, R., Sudarsky, D., & Sharp, C. (1997). A Nongray Theory of Extrasolar Giant Planets and Brown Dwarfs. , 491, 856–875.

Calvet, N. & Gullbring, E. (1998). The Structure and Emission of the Accretion Shock in T Tauri Stars. , 509, 802–818.

Carroll, B. & Ostlie, D. (2007). *An Introduction to Modern Astrophysics*. Pearson Addison-Wesley.

Chauvin, G., Lagrange, A.-M., Dumas, C., Zuckerman, B., Mouillet, D., Song, I., Beuzit, J.-L., & Lowrance, P. (2004). A giant planet candidate near a young brown dwarf. Direct VLT/NACO observations using IR wavefront sensing. , 425, L29–L32.

Chen, H. & Rogers, L. A. (2016). Evolutionary Analysis of Gaseous Sub-Neptune-mass Planets with MESA. , 831, 180.

Close, L. M., Zuckerman, B., Song, I., Barman, T., Marois, C., Rice, E. L., Siegler, N., Macintosh, B., Becklin, E. E., Campbell, R., Lyke, J. E., Conrad, A., & Mignant, D. L. (2007). The wide brown dwarf binary oph 1622–2405 and discovery of a wide, low-mass binary in ophiuchus (oph 1623–2402): A new class of young evaporating wide binaries? *The Astrophysical Journal*, 660(2), 1492.

Commerçon, B., Audit, E., Chabrier, G., & Chièze, J.-P. (2011). Physical and radiative properties of the first-core accretion shock. , 530, A13.

Currie, T., Burrows, A., Madhusudhan, N., Fukagawa, M., Girard, J. H., Dawson, R., Murray-Clay, R., Kenyon, S., Kuchner, M., Matsumura, S., Jayawardhana, R., Chambers, J., & Bromley, B. (2013). A Combined Very Large Telescope and Gemini Study of the Atmosphere of the Directly Imaged Planet, β Pictoris b. , 776, 15.

Currie, T., Cloutier, R., Brittain, S., Grady, C., Burrows, A., Muto, T., Kenyon, S. J., & Kuchner, M. J. (2015). Resolving the HD 100546 Protoplanetary System with the Gemini Planet Imager: Evidence for Multiple Forming, Accreting Planets. , 814, L27.

Currie, T., Daemgen, S., Debes, J., Lafreniere, D., Itoh, Y., Jayawardhana, R., Ratzka, T., & Correia, S. (2014a). Direct Imaging and Spectroscopy of a Candidate Companion Below/Near the Deuterium-burning Limit in the Young Binary Star System, ROXs 42B. , 780, L30.

Currie, T., Muto, T., Kudo, T., Honda, M., Brandt, T. D., Grady, C., Fukagawa, M., Burrows, A., Janson, M., Kuzuhara, M., McElwain, M. W., Follette, K., Hashimoto, J., Henning, T., Kandori, R., Kusakabe, N., Kwon, J., Mede, K., Morino, J.-i., Nishikawa, J., Pyo, T.-S., Serabyn, G., Suenaga, T., Takahashi, Y., Wisniewski, J., & Tamura, M. (2014b). Recovery of the Candidate Protoplanet HD 100546 b with Gemini/NICI and Detection of Additional (Planet-induced?) Disk Structure at Small Separations. , 796, L30.

D'Orazi, V., Desidera, S., Gratton, R. G., Lanza, A. F., Messina, S., Andrievsky, S. M., Korotin, S., Benatti, S., Bonnefoy, M., Covino, E., & Janson, M. (2017). A critical reassessment of the fundamental properties of GJ 504: chemical composition and age. , 598, A19.

Fortney, J. J., Marley, M. S., Hubickyj, O., Bodenheimer, P., & Lissauer, J. J. (2005). Young Jupiters are faint: new models of the early evolution of giant planets. *Astronomische Nachrichten*, 326, 925–929.

Freedman, R. S., Marley, M. S., & Lodders, K. (2008). Line and Mean Opacities for Ultracool Dwarfs and Extrasolar Planets. , 174, 504–513.

Fuhrmann, K. & Chini, R. (2015). On the age of Gliese 504. , 806, 163.

Garufi, A., Quanz, S. P., Schmid, H. M., Mulders, G. D., Avenhaus, H., Boccaletti, A., Ginski, C., Langlois, M., Stolker, T., Augereau, J.-C., Benisty, M., Lopez, B., Dominik, C., Gratton, R., Henning, T., Janson, M., Ménard, F., Meyer, M. R., Pinte, C., Sissa, E., Vigan, A., Zurlo, A., Bazzon, A., Buenzli, E., Bonnefoy, M., Brandner, W., Chauvin, G., Cheetham, A., Cudel, M., Desidera, S., Feldt, M., Galicher, R., Kasper, M., Lagrange, A.-M., Lannier, J., Maire, A. L., Mesa, D., Mouillet, D., Peretti,

S., Perrot, C., Salter, G., & Wildi, F. (2016). The SPHERE view of the planet-forming disk around HD 100546. , 588, A8.

Goldreich, P. & Ward, W. R. (1973). The Formation of Planetesimals. , 183, 1051–1062.

Hansen, C., Kawaler, S., & Trimble, V. (2012). *Stellar Interiors: Physical Principles, Structure, and Evolution*. Astronomy and Astrophysics Library. Springer New York.

Hartman, J. D., Bakos, G. Á., Torres, G., Latham, D. W., Kovács, G., Béky, B., Quinn, S. N., Mazeh, T., Shporer, A., Marcy, G. W., Howard, A. W., Fischer, D. A., Johnson, J. A., Esquerdo, G. A., Noyes, R. W., Sasselov, D. D., Stefanik, R. P., Fernandez, J. M., Szklenár, T., Lázár, J., Papp, I., & Sári, P. (2011). HAT-P-32b and HAT-P-33b: Two Highly Inflated Hot Jupiters Transiting High-jitter Stars. , 742, 59.

Hartmann, L., Cassen, P., & Kenyon, S. J. (1997). Disk Accretion and the Stellar Birthline. , 475, 770–785.

Helled, R. & Stevenson, D. (2017). The fuzziness of giant planets' cores. *ArXiv e-prints*.

Hill, T. L. (1986). *An Introduction to Statistical Thermodynamics (Dover Books on Physics)*. Dover Publications.

Huang, X. & Cumming, A. (2012). Ohmic Dissipation in the Interiors of Hot Jupiters. , 757, 47.

Hubeny, I. & Mihalas, D. (2014). *Theory of Stellar Atmospheres*.

Hubickyj, O., Bodenheimer, P., & Lissauer, J. J. (2005). Accretion of the gaseous envelope of Jupiter around a 5 10 Earth-mass core. , 179, 415–431.

Kuiper, G. P. (1951). On the Origin of the Solar System. *Proceedings of the National Academy of Science*, 37, 1–14.

Kuzuhara, M., Tamura, M., Kudo, T., Janson, M., Kandori, R., Brandt, T. D., Thalmann, C., Spiegel, D., Biller, B., Carson, J., Hori, Y., Suzuki, R., Burrows, A., Henning, T., Turner, E. L., McElwain, M. W., Moro-Martín, A., Suenaga, T., Takahashi, Y. H., Kwon, J., Lucas, P., Abe, L., Brandner, W., Egner, S., Feldt, M., Fujiwara, H., Goto, M., Grady, C. A., Guyon, O., Hashimoto, J., Hayano, Y., Hayashi, M., Hayashi, S. S., Hodapp, K. W., Ishii, M., Iye, M., Knapp, G. R., Matsuo, T., Mayama, S., Miyama, S., Morino, J.-I., Nishikawa, J., Nishimura, T., Kotani, T., Kusakabe, N., Pyo, T.-S., Serabyn, E., Suto, H., Takami, M., Takato, N., Terada, H., Tomono, D., Watanabe, M., Wisniewski, J. P., Yamada, T., Takami, H., & Usuda, T. (2013). Direct Imaging of a Cold Jovian Exoplanet in Orbit around the Sun-like Star GJ 504. , 774, 11.

Lagrange, A.-M., Bonnefoy, M., Chauvin, G., Apai, D., Ehrenreich, D., Boccaletti, A., Gratadour, D., Rouan, D., Mouillet, D., Lacour, S., & Kasper, M. (2010). A Giant Planet Imaged in the Disk of the Young Star β Pictoris. *Science*, 329, 57.

Lagrange, A.-M., Kasper, M., Boccaletti, A., Chauvin, G., Gratadour, D., Fusco, T., Ehrenreich, D., Apai, D., Mouillet, D., & Rouan, D. (2009). Constraining the orbit of the possible companion to β Pictoris. New deep imaging observations. , 506, 927–934.

Leconte, J. & Chabrier, G. (2012). A new vision of giant planet interiors: Impact of double diffusive convection. , 540, A20.

Ledoux, P. (1947). Stellar Models with Convection and with Discontinuity of the Mean Molecular Weight. , 105, 305.

Lissauer, J. J., Hubickyj, O., D'Angelo, G., & Bodenheimer, P. (2009). Models of Jupiter's growth incorporating thermal and hydrodynamic constraints. , 199, 338–350.

Macintosh, B., Graham, J. R., Barman, T., De Rosa, R. J., Konopacky, Q., Marley, M. S., Marois, C., Nielsen, E. L., Pueyo, L., Rajan, A., Rameau, J., Saumon, D., Wang, J. J., Patience, J., Ammons, M.,

Arriaga, P., Artigau, E., Beckwith, S., Brewster, J., Bruzzone, S., Bulger, J., Burningham, B., Burrows, A. S., Chen, C., Chiang, E., Chilcote, J. K., Dawson, R. I., Dong, R., Doyon, R., Draper, Z. H., Duchêne, G., Esposito, T. M., Fabrycky, D., Fitzgerald, M. P., Follette, K. B., Fortney, J. J., Gerard, B., Goodsell, S., Greenbaum, A. Z., Hibon, P., Hinkley, S., Cotten, T. H., Hung, L.-W., Ingraham, P., Johnson-Groh, M., Kalas, P., Lafreniere, D., Larkin, J. E., Lee, J., Line, M., Long, D., Maire, J., Marchis, F., Matthews, B. C., Max, C. E., Metchev, S., Millar-Blanchaer, M. A., Mittal, T., Morley, C. V., Morzinski, K. M., Murray-Clay, R., Oppenheimer, R., Palmer, D. W., Patel, R., Perrin, M. D., Poyneer, L. A., Rafikov, R. R., Rantakyrö, F. T., Rice, E. L., Rojo, P., Rudy, A. R., Ruffio, J.-B., Ruiz, M. T., Sadakuni, N., Saddlemyer, L., Salama, M., Savransky, D., Schneider, A. C., Sivaramakrishnan, A., Song, I., Soummer, R., Thomas, S., Vasisht, G., Wallace, J. K., Ward-Duong, K., Wiktorowicz, S. J., Wolff, S. G., & Zuckerman, B. (2015). Discovery and spectroscopy of the young jovian planet 51 Eri b with the Gemini Planet Imager. *Science*, 350, 64–67.

Marleau, G.-D. & Cumming, A. (2014). Constraining the initial entropy of directly detected exoplanets. , 437, 1378–1399.

Marleau, G.-D., Klahr, H., Kuiper, R., & Mordasini, C. (2017). The Planetary Accretion Shock. I. Framework for Radiation-hydrodynamical Simulations and First Results. , 836, 221.

Marley, M. S., Fortney, J. J., Hubickyj, O., Bodenheimer, P., & Lissauer, J. J. (2007). On the Luminosity of Young Jupiters. , 655, 541–549.

Marois, C., Macintosh, B., Barman, T., Zuckerman, B., Song, I., Patience, J., Lafrenière, D., & Doyon, R. (2008). Direct Imaging of Multiple Planets Orbiting the Star HR 8799. *Science*, 322, 1348.

Marois, C., Zuckerman, B., Konopacky, Q. M., Macintosh, B., & Barman, T. (2010). Images of a fourth planet orbiting HR 8799. , 468, 1080–1083.

Mizuno, H. (1980). Formation of the Giant Planets. *Progress of Theoretical Physics*, 64, 544–557.

Mordasini, C. (2013). Luminosity of young Jupiters revisited. Massive cores make hot planets. , 558, A113.

Mordasini, C., Alibert, Y., Klahr, H., & Henning, T. (2012). Characterization of exoplanets from their formation. I. Models of combined planet formation and evolution. , 547, A111.

Mordasini, C., Klahr, H., Alibert, Y., Miller, N., & Henning, T. (2014). Grain opacity and the bulk composition of extrasolar planets. I. Results from scaling the ISM opacity. , 566, A141.

Mordasini, C., Mollière, P., Dittkrist, K.-M., Jin, S., & Alibert, Y. (2015). Global models of planet formation and evolution. *International Journal of Astrobiology*, 14, 201–232.

Nettelmann, N., Fortney, J. J., Moore, K., & Mankovich, C. (2015). An exploration of double diffusive convection in Jupiter as a result of hydrogen-helium phase separation. , 447, 3422–3441.

Neuhäuser, R. & Schmidt, T. O. B. (2012). Direct Imaging of Extra-solar Planets - Homogeneous Comparison of Detected Planets and Candidates. *ArXiv e-prints*.

Ormel, C. W. (2014). An Atmospheric Structure Equation for Grain Growth. , 789, L18.

Owen, J. E. & Menou, K. (2016). Disk-fed Giant Planet Formation. , 819, L14.

Paxton, B., Bildsten, L., Dotter, A., Herwig, F., Lesaffre, P., & Timmes, F. (2011). Modules for Experiments in Stellar Astrophysics (MESA). , 192, 3.

Paxton, B., Cantiello, M., Arras, P., Bildsten, L., Brown, E. F., Dotter, A., Mankovich, C., Montgomery, M. H., Stello, D., Timmes, F. X., & Townsend, R. (2013). Modules for Experiments in Stellar Astrophysics (MESA): Planets, Oscillations, Rotation, and Massive Stars. , 208, 4.

Paxton, B., Marchant, P., Schwab, J., Bauer, E. B., Bildsten, L., Cantiello, M., Dessart, L., Farmer, R., Hu, H., Langer, N., Townsend, R. H. D., Townsley, D. M., & Timmes, F. X. (2015). Modules for Experiments in Stellar Astrophysics (MESA): Binaries, Pulsations, and Explosions. , 220, 15.

Pollack, J. B., Grossman, A. S., Moore, R., & Graboske, H. C. (1977). A calculation of saturn's gravitational contraction history. *Icarus*, 30(1), 111 – 128.

Pollack, J. B., Hubickyj, O., Bodenheimer, P., Lissauer, J. J., Podolak, M., & Greenzweig, Y. (1996). Formation of the Giant Planets by Concurrent Accretion of Solids and Gas. , 124, 62–85.

Prialnik, D. & Livio, M. (1985). The outcome of accretion on to a fully convective star Expansion or contraction? , 216, 37–52.

Quanz, S. P., Amara, A., Meyer, M. R., Girard, J. H., Kenworthy, M. A., & Kasper, M. (2015). Confirmation and Characterization of the Protoplanet HD 100546 bDirect Evidence for Gas Giant Planet Formation at 50 AU. , 807, 64.

Quanz, S. P., Amara, A., Meyer, M. R., Kenworthy, M. A., Kasper, M., & Girard, J. H. (2013). A Young Protoplanet Candidate Embedded in the Circumstellar Disk of HD 100546. , 766, L1.

Rameau, J., Chauvin, G., Lagrange, A.-M., Boccaletti, A., Quanz, S. P., Bonnefoy, M., Girard, J. H., Delorme, P., Desidera, S., Klahr, H., Mordasini, C., Dumas, C., & Bonavita, M. (2013). Discovery of a Probable 4-5 Jupiter-mass Exoplanet to HD 95086 by Direct Imaging. , 772, L15.

Safronov, V. S. (1972). *Evolution of the protoplanetary cloud and formation of the earth and planets.*

Sallum, S., Follette, K. B., Eisner, J. A., Close, L. M., Hinz, P., Kratter, K., Males, J., Skemer, A., Macintosh, B., Tuthill, P., Bailey, V., Defrère, D., Morzinski, K., Rodigas, T., Spalding, E., Vaz, A., & Weinberger, A. J. (2015). Accreting protoplanets in the LkCa 15 transition disk. , 527, 342–344.

Saumon, D., Chabrier, G., & van Horn, H. M. (1995). An Equation of State for Low-Mass Stars and Giant Planets. , 99, 713.

Schneider, J., Dedieu, C., Le Sidaner, P., Savalle, R., & Zolotukhin, I. (2011). Defining and cataloging exoplanets: the exoplanet.eu database. , 532, A79.

Schwarzschild, K. (1906). On the equilibrium of the Sun's atmosphere. *Nachrichten von der Königlichen Gesellschaft der Wissenschaften zu Göttingen. Math.-phys. Klasse, 195, p. 41-53*, 195, 41–53.

Siess, L., Forestini, M., & Bertout, C. (1997). Physics of accretion onto young stars. II. Structure and evolution of accreting stars. , 326, 1001–1012.

Spiegel, D. S. & Burrows, A. (2012). Spectral and Photometric Diagnostics of Giant Planet Formation Scenarios. , 745, 174.

Stahler, S. W. (1988). Deuterium and the stellar birthline. , 332, 804–825.

Stahler, S. W., Shu, F. H., & Taam, R. E. (1980). The evolution of protostars. I - Global formulation and results. , 241, 637–654.

Stevenson, D. J. (1982). Formation of the giant planets. , 30, 755–764.

Todorov, K. O., Luhman, K. L., Konopacky, Q. M., McLeod, K. K., Apai, D., Ghez, A. M., Pascucci, I., & Robberto, M. (2014). A Search for Companions to Brown Dwarfs in the Taurus and Chamaeleon Star-Forming Regions. , 788, 40.

Wagner, K., Apai, D., Kasper, M., Kratter, K., McClure, M., Robberto, M., & Beuzit, J.-L. (2016). Direct imaging discovery of a Jovian exoplanet within a triple-star system. *Science*, 353, 673–678.

Wolszczan, A. (1994). Confirmation of Earth-Mass Planets Orbiting the Millisecond Pulsar PSR B1257+12. *Science*, 264, 538–542.

Wolszczan, A. & Frail, D. A. (1992). A planetary system around the millisecond pulsar PSR1257 + 12. , 355, 145–147.

Wu, Y. & Lithwick, Y. (2013). Ohmic Heating Suspends, Not Reverses, the Cooling Contraction of Hot Jupiters. , 763, 13.